Solar Phys (2016) 291:2281–2328
DOI 10.1007/s11207-016-0964-4

Spectroscopy at the Solar Limb: II. Are Spicules Heated to Coronal Temperatures?

C. Beck[1] · R. Rezaei[2] · K.G. Puschmann[3] · D. Fabbian[4,5,6]

Received: 14 September 2015 / Accepted: 25 July 2016 / Published online: 18 August 2016

Abstract Spicules of the so-called type II were suggested to be relevant for coronal heating because of their ubiquity on the solar surface and their eventual extension into the corona. We investigate whether solar spicules are heated to transition-region or coronal temperatures and reach coronal heights ($\gg 6$ Mm) using multiwavelength observations of limb spicules in different chromospheric spectral lines (Ca II H, Hϵ, Hα, Ca II IR at 854.2 nm, He I at 1083 nm) taken with slit spectrographs and imaging spectrometers. We determine the line width of spectrally resolved line profiles in individual spicules and throughout the field of view, and estimate the maximal height that different types of off-limb features reach. We derive estimates of the kinetic temperature and the non-thermal velocity from the line width of spectral lines from different chemical elements. We find that most regular, *i.e.* thin and elongated, spicules reach a height of at most about 6 Mm above the solar limb. The majority of features found at larger heights are irregularly shaped with a significantly larger lateral extension, of up to a few Mm, than spicules. Both individual and average line profiles in all spectral lines show a decrease in their line width with height above the limb with very few exceptions. The kinetic temperature and the non-thermal velocity decrease with height above the limb. We find no indications that the spicules in our data reach coronal heights or transition-region or coronal temperatures.

Keywords Sun: chromosphere · Techniques: spectroscopic · Line: profiles

Electronic supplementary material The online version of this article (doi:10.1007/s11207-016-0964-4) contains supplementary material, which is available to authorized users.

✉ C. Beck
cbeck@nso.edu

1 National Solar Observatory (NSO), 88349 Sunspot, NM, USA

2 Kiepenheuer-Institut für Sonnenphysik (KIS), 79104 Freiburg, Germany

3 Martinstr. 64, 64285 Darmstadt, Germany

4 Instituto de Astrofísica de Canarias (IAC), 38205 La Laguna, Tenerife, Spain

5 Departamento de Astrofísica, Universidad de La Laguna (ULL), 38206 La Laguna, Tenerife, Spain

6 Max-Planck-Institut für Sonnensytemforschung (MPS), 37077 Göttingen, Germany

1. Introduction

Most of the processes on the solar surface, with the exception of convective energy transport and solar oscillations, are driven by magnetic fields. At the photospheric level, the gas density is high enough for the kinetic pressure to dominate magnetic pressure. In contrast, magnetic energy density is higher than kinetic energy density in the chromosphere and the corona. While the spatial structuring in the photosphere is given by the granulation pattern, the shape of the solar chromosphere is markedly different. One key component of the chromosphere are the so-called spicules: hair-like, thin, elongated features observed at the solar limb in strong chromospheric lines such as Hα (*e.g.* Roberts, 1945, or the reviews of Beckers, 1968 (BE68), Sterling, 2000, and Tsiropoula *et al.*, 2012). Some spicules are bright in extreme-ultraviolet (EUV) lines as well as in Hα, indicating an extension up to coronal heights. Spicules are transient features that apparently shoot up from the solar limb to a height of a few Mm (*e.g.* Zirker, 1962b), to disappear from sight again after some tens of seconds to a few minutes (BE68; De Pontieu *et al.*, 2007a). Because of possible projection effects, it is unclear whether the apparent motions seen at the limb are caused by mass motions or waves. There are controversial observational arguments whether spicules fade away *in situ* or return to the solar surface (Suematsu, Wang, and Zirin, 1995; Pasachoff, Jacobson, and Sterling, 2009; Sterling, Moore, and DeForest, 2010; Anan *et al.*, 2010; Pereira, De Pontieu, and Carlsson, 2012; Zhang *et al.*, 2012). Pasachoff, Noyes, and Beckers (1968) and De Pontieu *et al.* (2012) suggested that spicules undergo twisting and torsional motions while they evolve.

On the solar disk, dark and bright mottles and fibrils are believed to be the counterpart of limb spicules (Beckers, 1972). There is no canonical proof that mottles or fibrils are spicules seen on-disk, but are probably at least related (Grossmann-Doerth and Schmidt, 1992; Tsiropoula and Schmieder, 1997; Suematsu, 1998; Zachariadis *et al.*, 1999; Langangen *et al.*, 2008; Rouppe van der Voort *et al.*, 2009). Mottles cluster at the boundary of supergranular cells. The most reliable identification of the on-disk counterpart of spicules is through the corresponding line-of-sight (LOS) velocities (*e.g.* Sekse, Rouppe van der Voort, and De Pontieu, 2012, 2013). There is no agreement if there are any spicules in plage regions (Shibata and Suematsu, 1982; Zirin, 1988; De Pontieu *et al.*, 2007a, but see also Anan *et al.*, 2010).

The typical length of spicules is from 5 – 10 Mm, while their width ranges from 1 Mm down to the resolution limit of the respective observations, *i.e.* as small as $0\farcs1$ (Beckers, 1972; Nishikawa, 1988; Suematsu *et al.*, 2007, 2008). Hence, the aspect ratio of the hair-like spicular structures is about ten or more. They are usually inclined with respect to the local vertical by about 10 – 40 degrees (Pasachoff, Jacobson, and Sterling, 2009). In polar regions, spicules are close to vertical and show a larger extension (BE68). The "traditional" spicules have a lifetime of some 5 to 15 min. In Hα, they show a velocity of some 25 km s^{-1} and typical chromospheric temperatures of about 10 000 K (Zirker, 1962a; Beckers, 1972; Matsuno and Hirayama, 1988; Makita, 2003). At low spatial resolution, they appear to emanate from unipolar regions (Suematsu, Wang, and Zirin, 1995). Finally, it is unclear whether spicules rise smoothly or intermittently.

The spectral signature of spicules varies in the red and blue wings of the Hα line. Beckers (1972) noted that this can be due to a variation in Doppler shift or line width (see also Shoji *et al.*, 2010). The height and thickness of spicules changes between, *e.g.*, Hα and Ca II H and K. This difference is the joint action of different spatial resolution and smoothing effects at different wavelengths as well as a physical difference in the response of the two lines.

The interest in spicules has been revived by new observations with improved spatial resolution, higher temporal cadence, or enhanced spectropolarimetric sensitivity. One major source for data of the first two categories is the *Solar Optical Telescope* (Tsuneta *et al.*, 2008) and its instrumentation onboard the *Hinode* satellite (Kosugi *et al.*, 2007). Observations with the 0.3 nm wide Ca II H interference filter of *Hinode* have been used to address the structure and evolution of spicules and larger-scale filaments and prominences near the limb (*e.g.* Suematsu *et al.*, 2007; Berger *et al.*, 2008), although the two-dimensional (2D) imaging data provide only apparent motions in the sky plane in intensity images. The *Hinode* Ca filter also covers the chromospheric emission of the Hε line, which contributes up to 30 % to the filter intensity near the solar limb (Beck, Rezaei, and Puschmann, 2013). Another source of fast, high-resolution imaging at multiple wavelengths is the *Rapid Oscillations in the Solar Atmosphere* (ROSA: Jess *et al.*, 2010) instrument at the *Dunn Solar Telescope* (DST: Dunn, 1964; Dunn and Smartt, 1991), which has been used to study, *e.g.*, oscillations inside of spicules (Jess *et al.*, 2012).

The information content of high-resolution imaging data was extended to high-resolution imaging spectroscopy with the *Interferometric Bidimensional Spectrometer* (IBIS: Cavallini, 2006; Reardon and Cavallini, 2008) at the DST, the *GREGOR Fabry–Pérot Interferometer* (GFPI: Puschmann *et al.*, 2006, 2007, 2012a,b,c, 2013; Puschmann, 2016b) at the German *Vacuum Tower Telescope* (VTT: Schroeter, Soltau, and Wiehr, 1985), or the *Crisp Imaging Spectro-Polarimeter* (CRISP: Scharmer *et al.*, 2008) at the *Swedish 1m Solar Telescope* (SST: Scharmer *et al.*, 2003). These data of high spatial resolution in Hα and the Ca II infrared (IR) line at 854 nm have been used to determine the properties of spicules or related features off the limb (Pasachoff, Jacobson, and Sterling, 2009; De Pontieu *et al.*, 2012) or on the solar disk (Langangen *et al.*, 2008; Sánchez-Andrade Nuño *et al.*, 2008; Rouppe van der Voort *et al.*, 2009; Sekse, Rouppe van der Voort, and De Pontieu, 2013).

Data with enhanced polarimetric sensitivity were provided by the *Advanced Stokes Polarimeter* (ASP: Skumanich *et al.*, 1997) at the DST in the He I D_3 line (*e.g.* Casini *et al.*, 2003; López Ariste and Casini, 2005), the *Tenerife Infrared Polarimeter* (TIP: Mártinez Pillet *et al.*, 1999; Collados *et al.*, 2007) at the VTT in the He I line at 1083 nm (*e.g.* Centeno, Trujillo Bueno, and Asensio Ramos, 2010; Martínez González *et al.*, 2012), the *Spectro-Polarimeter for Infrared and Optical Regions* (SPINOR: Socas-Navarro *et al.*, 2006) at the DST in He I at 1083 nm and the Ca II infrared (IR) lines (Socas-Navarro and Elmore, 2005), the polarimetric mode of the *Télescope Héliographique pour l'Etude du Magnétisme et des Instabilités Solaires* (THEMIS) (López Ariste, Rayrole, and Semel, 2000; Paletou *et al.*, 2001), or the *Zürich Imaging Polarimeter* (ZIMPOL: Gandorfer *et al.*, 2004) at the *Gregory–Coudé Telescope* in Locarno in the He I D_3 line (*e.g.* Ramelli *et al.*, 2006).

The new data allowed old observational and theoretical results on spicules to be revised. With the spectropolarimetric observations, the magnetic field strength in spicules could be determined to be between 10 G and 50 G (Trujillo Bueno *et al.*, 2005; Centeno, Trujillo Bueno, and Asensio Ramos, 2010). Orozco Suárez, Asensio Ramos, and Trujillo Bueno (2015) found a decrease in magnetic field strength from 80 G at the limb to 30 G at a height of 3 Mm above it. De Pontieu *et al.* (2007b) introduced two types of spicules based on their lifetime (15 min for type I *vs.* 2 min or shorter for type II; see also Rouppe van der Voort *et al.*, 2009), where short-lived spicules are also generally thinner and show faster apparent velocities than traditional spicules, although BE68 previously described two types of spicules differing in their line widths. De Pontieu *et al.* (2007b) stated that most of the type II spicules do not show a descent, but fade from sight *in situ*, which might be caused by a rapid heating to transition-region and coronal temperatures. It is unclear at present whether these new and old two types might correspond to the same classification and in which way type I

and type II spicules truly differ. Avery (1970) explained the two types of spicules defined by BE68 as being solely caused by different (or absent) rotation. Pereira, De Pontieu, and Carlsson (2012) suggested that the two types of spicules of BE68 would fall into the new type I category, as defined by De Pontieu *et al.* (2007b), whereas the new type II spicules are thought to have been undetectable at the temporal and spatial resolution of older observations (*cf.* also Pereira, De Pontieu, and Carlsson, 2013). Zhang *et al.* (2012) reanalyzed the data used by De Pontieu *et al.* (2007b) and found both an ascending and descending phase for most of their spicule examples. The authors questioned the existence of type II spicules as being somehow different from the classical type I spicules (see also the discussion in Skogsrud *et al.*, 2015).

There are suggestions that different mechanisms work on different types of spicules (Hammer *et al.*, 2008; Martínez-Sykora *et al.*, 2009) and various theoretical models have been proposed (Sterling, 2000, and references therein). These models have to provide a source of energy to support spicules against gravity, to accelerate them upwards, and to explain their elongated shape and temporal evolution. Candidates for the energy source are photospheric impulsive events (Hollweg, 1982; Suematsu *et al.*, 1982; De Pontieu, Erdélyi, and James, 2004) and energy sources that are related to magnetic fields, such as Alfvén waves (*e.g.* De Pontieu and Haerendel, 1998; Kudoh and Shibata, 1999; Hansteen *et al.*, 2006; Rouppe van der Voort *et al.*, 2007), small-scale reconnection events (Heggland, De Pontieu, and Hansteen, 2009; Yurchyshyn, Abramenko, and Goode, 2013), or localized currents that accelerate material by the Lorentz force (Martínez-Sykora, Hansteen, and Moreno-Insertis, 2011; Goodman, 2012). There are indications that the height extension of spicules is affected by the transition-region height and *vice versa* (Shibata and Suematsu, 1982; Guerreiro, Carlsson, and Hansteen, 2013). Magnetohydrodynamic (MHD) wave models of spicules (Kulidzanishvili and Zhugzhda, 1983; Kukhianidze, Zaqarashvili, and Khutsishvili, 2006; He *et al.*, 2009) are motivated by observations of oscillations and observed Doppler shifts (the so-called line tilt) that again date back to BE68 and before. Despite many observational constraints, no canonical model for spicules could be derived that matched their principal observed dynamical properties.

Because spicules, or more precisely, type II spicules according to the new definition, were found to be abundantly present on the solar surface, they might transport a significant amount of energy into the corona (De Pontieu *et al.*, 2009; Tian *et al.*, 2014; Henriques *et al.*, 2016). As discussed by Judge *et al.* (2012), this idea of a coronal energy input from the chromosphere has been suggested earlier (Athay and Holzer, 1982; Athay, 2000), but there were only indirect proofs for this process, *e.g.*, the amount and direction of (vertical) net mass flows (Pneuman and Kopp, 1978). Most of the argumentation for a relation between the chromospheric spicules and the transition region or corona was based on the dynamic evolution and the dynamic properties of spicules (LOS velocities, acceleration or deceleration at the disk center and near the limb; *e.g.* McIntosh and De Pontieu, 2009). Madjarska, Vanninathan, and Doyle (2011) were unable to find coronal counterparts to three large-scale macrospicules (*cf.* Bohlin *et al.*, 1975; Pike and Harrison, 1997; Kamio *et al.*, 2010; Scullion, Doyle, and Erdélyi, 2010; Murawski, Srivastava, and Zaqarashvili, 2011) seen in Ca II H imaging from *Hinode*. Pereira *et al.* (2014) and Rouppe van der Voort *et al.* (2015) found counterparts to spicules in transition-region lines at the limb and on the disk, respectively.

Here, we investigate a possible connection of spicular material to atmospheric layers above the chromosphere by determining the greatest reached height above the solar limb attained by different types of features and by deriving the height dependence of the line width in various chromospheric spectral lines. Assuming a heating process from chromospheric

(5000 to 20 000 K) to transition-region temperatures ($> 10^5$ K) during their rise, the line width in resolved spectra is expected to increase with height when the upper end of spicules is heated.

Section 2 describes the various data sets covering several chromospheric spectral lines (Ca II H, Hε, Hα, Ca II IR at 854.2 nm, He I at 1083 nm) in one-dimensional (1D) and two-dimensional (2D) spectroscopy. The data reduction and quantities derived from the spectra are explained in Section 3. The results of Section 4 are summarized in Section 5 and discussed in Section 6. Section 7 provides our conclusions. Appendix A shows several examples of time series of imaging spectroscopy in Hα. Appendix B discusses the significance limits of the profiles and the analysis approach, while Appendix C shows additional examples of spectrograph observations.

2. Observations

For the simultaneous observations of up to five chromospheric spectral lines in four different wavelength regimes from the near-ultraviolet (UV) to the near-IR, we used different combinations of the post-focus instruments available at the VTT at that time: the main echelle spectrograph for spectropolarimetric observations of He I 1083 nm with TIP and simultaneous spectroscopy of Ca II IR at 854.2 nm with a PCO 4000 camera, the *Triple Etalon Solar Spectrometer* (TESOS: Kentischer *et al.*, 1998; Tritschler *et al.*, 2002) for imaging spectroscopy of Hα, and the *Polarimetric Littrow Spectrograph* (POLIS: Beck *et al.*, 2005) for spectroscopic observations of Ca II H, Hε, and Hα. The two combinations of the instruments that we used are described in detail in Beck and Rezaei (2012). Their main difference is the usage of TESOS for 2D spectroscopy in Hα in 2010 (setup 1), while in 2011 all lines were observed with slit-spectrographs (setup 2). Table 1 lists the spectral and spatial characteristics of the data that only vary for Ca II H and Hα.

In setup 1, TESOS was run without direct synchronization to the scanning. We set it to a continuous observing mode as soon as the adaptive optics (AO) was locked near the limb.

Table 1 Spatial and spectral characteristics of the data.

Line	Dispersion [pm/pixel]	Wavelength [nm]	Slit width [″]	Spatial sampling [″/pixel]
Setup 1 and 2: TIP and echelle spectrograph				
He I	1.1	1082.34 – 1083.45	0.36	0.18
Ca II IR	0.82	853.45 – 855.10	0.36	0.18
Setup 1: TESOS and POLIS				
Hα[1]	4.9	656.16 – 656.39	–	0.09
Ca II H[2]	1.45	395.86 – 398.75	0.5	0.22
Setup 2: POLIS				
Hα[2]	2	654.22 – 657.61	0.5	0.22
Ca II H[3]	1.92	396.34 – 396.95	0.5	0.292
Setup 3: GFPI				
Hα	11.1	656.17 – 656.40	–	0.11

[1]TESOS. [2]PCO 4000 in POLIS. [3]Default POLIS CCD.

Table 2 Observation settings.

	Number				
	1	2	3	4	5
Date	30 June 2010	01 July 2010	01 July 2010	02 July 2010	12 July 2011
Time [UT]	07:48 – 08:08	07:56 – 08:24	08:59 – 09:19	08:11 – 08:24	07:50 – 08:14
Pos. x''/y''	−864/349	−868/293	−868/293	−354/ − 836	−933/172
Type	QS map	QS map	QS map	QS ts	AR map
t [s]	10	60	6	6	8
Steps[1]	100 × 0.3	25 × 0.3	150 × 0.3	20 × 0.5 × 5	150 × 0.36
Duration [min]	20	28	19	13	25
Cadence [s]	30[2]	20[2]	20[2]	156[3]	–
Angle[4] [deg]	90	90	90	0	90
Setup[5]	1	1	1	1	2

	Number
	6
Date	04 May 2005
Time [UT]	08:47 – 09:02
Pos. x''/y''	South Pole
Type	QS ts
t [ms]	20
Steps	39
Duration [min]	15
Cadence [s]	≈ 20
Setup[5]	3

[1]Number of steps *per* step width in arcseconds (*per* number of repetitions of the scan where applicable). [2]Cadence of TESOS spectra. [3]Cadence of slit-spectrograph spectra. [4]Angle relative to the solar limb. [5]Setup 1 uses TIP, TESOS, and POLIS, setup 2 uses TIP and POLIS, and setup 3 uses GFPI.

The cadence of TESOS was either about 20 or 30 s, depending on whether a second line (Mg I at 517 nm) was recorded in addition to Hα. The TESOS field of view (FOV) was circular with a diameter of 40″.

In both setups, we aimed for observations of spicules in three different observing modes of the spectrograph instruments: large-area maps, time series (ts), and long-integrated (> 30 s) small-area maps. All three types of observations were made with the slit parallel and perpendicular to the limb. The fastest cadence in the slit-spectrograph data was 80 s, and the integration time *per* scan step [t] varied between 6 s and 2 min.

We finally selected only a subset of five specific observations for the current study. The corresponding settings are listed in Table 2. In all cases, the chromospheric spectral lines of He I at 1083 nm, Ca II IR at 854.2 nm, Hα at 656 nm, and Ca II H at 396.85 nm were observed simultaneously. In setup 1 (observations 1 to 4), Hε at 397 nm was also covered in the POLIS data and the Hα line was recorded with a 2D spectrometer, but only sampled within a limited spectral range. In setup 2 (observation 5), the spectral range around Hα was extended because of observing it with a slit spectrograph, but Hε was not covered anymore in the Ca II H spectra because the default Ca CCD of POLIS was used.

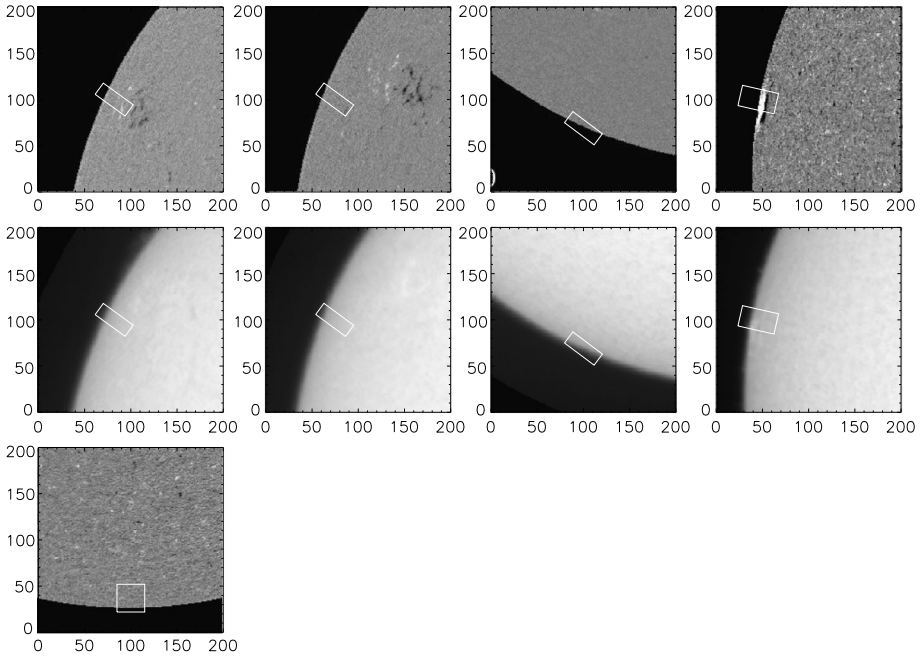

Figure 1 Location of the FOVs on full-disk LOS magnetograms and Hα images. Top row (second row), left to right: observations 1, 2 and 3, 4, and 5 overlaid on a magnetogram (Hα image). Bottom row: observation 6 overlaid on a magnetogram. The axis labels are in arcsecs.

In addition to the multiline observations described above, we used a time series of about 15 min obtained with the GFPI on 04 May 2005 at the VTT (setup 3) in the Hα line alone. The spectral line was sampled in 21 steps of 11 pm width with a cadence of about 22 s (Puschmann *et al.*, 2006). The spectra were reconstructed with the Multi-Object Multi-Frame Blind Deconvolution Technique (MOMFBD: Löfdahl, 2002; van Noort, Rouppe van der Voort, and Löfdahl, 2005) as part of the Imaging Spectropolarimetric Parallel-Organized Reconstruction Data Pipeline (ISPOR-DP), the GFPI data pipeline described in Puschmann and Beck (2011). These data have the highest spatial resolution in our sample. The spectra covered a similar wavelength range as the Hα spectra from TESOS, but had a coarser spectral sampling.

Figure 1 shows the locations of the FOVs of the observations overlaid on cutouts from LOS *Michelson Doppler Imaging* (MDI) magnetograms (observations 1 – 4 and 6) and *Helioseismic and Magnetic Imager* (HMI) magnetograms (observation 5), and from *Global Oscillation Network Group* (GONG) Hα images (all except for observation 6), respectively. All data except for observation 5 were taken in quiet-Sun (QS) areas, while observation 5 was taken in active region (AR) NOAA 11191. There are no discernible large-scale structures such as prominences in the Hα images that could have had an effect on the observations close to the limb. All observations benefited from the real-time correction of wavefront deformations by the *Kiepenheuer-Institut Adaptive Optics System* (KAOS: von der Lühe *et al.*, 2003). Apart from the observations in 2011, where a sunspot was located close to the limb, a facula was selected as adaptive optics (AO) lock-point. The latter was possible because at the VTT the light level in the AO wave-front sensor could be adjusted by a motorized gray

wedge and the AO software removed intensity gradients before the correlation of subapertures.

3. Data Reduction and Analysis

We corrected the spectra from all instruments for the dark current of the CCDs. The removal of flat-field defects had to be adjusted for each spectral line and instrument. In this section, we describe the additional data reduction steps or analysis methods that are particular for the off-limb data.

3.1. Stray-Light Correction

For observations on the solar disk, stray light contaminates the data with about 20 % of spurious light (*e.g.* Beck, Rezaei, and Fabbian, 2011; Beck *et al.*, 2013). For off-limb regions, the intrinsic intensities rapidly drop to below 20 % of the disk-center values (*e.g.* Beck and Rezaei, 2011), and thus stray light becomes critical. Some observational approaches enable minimizing stray light in off-limb observations, such as setting the spectrograph slit parallel to the limb (Centeno, Trujillo Bueno, and Asensio Ramos, 2010) or blocking the part of the slit (or FOV in general) that remains on the disk with an opaque cover similar to a coronagraph (Socas-Navarro and Elmore, 2005). However, some contamination of off-limb observations with light from the disk still cannot be avoided.

To reduce the stray-light contamination of the data, we used two different methods. The first was based on the theoretically correct approach of modeling the off-limb stray light from the intensities observed on the disk (Zwaan, 1965; Staveland, 1970; Mattig, 1983; Martinez Pillet, 1992; Beck, Rezaei, and Fabbian, 2011). A spatially and/or temporally averaged line profile was calculated for the on-disk region of the FOV that was farthest from the limb (about $10''-30''$) in each data set. Using the observed intensities on cuts across the limb, or a theoretical modeling or measurement of the spatial point-spread function (PSF), a suited stray-light fraction as a function of the limb distance can be determined (*cf.* Beck, Rezaei, and Fabbian, 2011; Löfdahl and Scharmer, 2012). The fraction is multiplied by the average on-disk profile and subtracted from the observed spectra. This method has the drawback that the region of the FOV that is still on the disk might not cover the full area from which the stray light originated, *e.g.*, the FOV would always need to cover the full solar disk in theory. This method thus commonly leaves some residuals far away from the limb because the average profile used is not identical to the real stray-light profile, but it provides a smooth stray-light correction across the limb without any discontinuities or intensity jumps at the limb location.

A second, more empirical approach can also be adopted for off-limb stray-light correction. The stray-light profile to be subtracted is determined from some off-limb region that is far away from the limb and from any true solar feature (*e.g.* Sánchez-Andrade Nuño *et al.*, 2007; Martínez González *et al.*, 2012). With this approach, the result of the stray-light contamination is used instead of the theoretical source of the stray light. The fraction of the stray-light profile to be subtracted can then be determined from the residual intensity at continuum wavelengths divided by the corresponding intensity in the stray-light profile. The advantage of this method is a good stray-light correction far away from the limb, but it typically shows a poorer correction close to the limb. It also creates a discontinuity in intensities at the location of the limb itself, which also has to be defined by some *ad hoc* criterion. Because we are mainly interested in the properties of off-limb spectra, we used

the second method for most data sets, except for those where a stray-light correction based on the first method had been applied to the data for previous studies. No stray-light correction was applied to the reconstructed GFPI spectra that showed little stray light after the deconvolution.

3.2. Determination of Line Parameters

Most of the data are either spatially or spectrally oversampled. To increase the signal-to-noise ratio, we therefore binned most of the spectra by two in the spatial and/or spectral dimension before deriving the line properties in individual profiles.

For all observations and all wavelength ranges, we used the average line profile from the on-disk region of the FOV that was farthest from the limb to determine an intensity normalization coefficient and any other necessary corrections, *e.g.*, linear or low-order intensity trends in the dispersion direction, that matched the average observed spectra to the corresponding Fourier transform spectrometer (FTS; Kurucz *et al.*, 1984; Neckel, 1999) solar atlas profiles. All other spectra of a given data set were then normalized and/or corrected with these values. For all on-disk and off-limb spectra, we derived the continuum intensity [I_c] from some continuum wavelength range and a generic line-core intensity [$I_{\rm core}$] from an integration over the line-core region in the spectra. The maps of I_c were used to coalign the observations in different wavelengths that showed offsets by differential refraction (*e.g.*, Appendix A of Beck *et al.*, 2008; Felipe *et al.*, 2010).

To determine the line width in individual spectra, we fitted single Gaussians to the line profiles. The central self-absorption in the line profiles disappears for heights larger than about 3 Mm above the limb, leaving a roughly Gaussian shape (see Figures 18 and 19 below). The spectral range to be analyzed was restricted each time to cover only the respective emission profile of a single line for the fit. The Ca II H spectra recorded with a PCO were the only case where two separate fits were performed to a single profile, *i.e.* one for Ca II H and one for Hε. The Gaussian fit yielded the central amplitude, the central position, and the full width at half maximum (FWHM) of the Gaussian. The position of the Gaussian was converted into the corresponding LOS velocity using the line-core position in the average profiles as zero-point reference.

As a cross-check of the width derived by the Gaussian fit, we also used a simpler method that only determined the highest intensity of the emission profile and the two positions where the intensity dropped to half of it. The FWHM is then directly given by the distance between these two positions.

The fit of a Gaussian function to the GFPI spectra worked less reliably because the outermost wavelength points in the blue and red wings often still sample the line emission without a clear drop of intensities, which also prevented us from determining the FWHM with the direct method. The line parameters for the GFPI spectra are thus not as well defined as for the other data.

3.3. Derivation of Kinetic Temperature and Non-thermal Line Width

The line width [$\Delta\lambda$] of emission lines formed in the optically thin regime can be described by

$$\Delta\lambda = \frac{\lambda}{c}\sqrt{\frac{2RT_{\rm kin}}{\mu} + v_{\rm non\text{-}th}^2}, \tag{1}$$

where λ is the central wavelength, c the speed of light, R the universal gas constant, $T_{\rm kin}$ the kinetic temperature, μ the molecular weight, and $v_{\rm non\text{-}th}$ any additional non-thermal line broadening (*e.g.* Tandberg-Hanssen, 1960; Bendlin, Wiehr, and Stellmacher, 1988). Magnetic broadening also contributes to the line width, but for typical chromospheric field strengths below 100 G (*e.g.* Centeno, Trujillo Bueno, and Asensio Ramos, 2010) it is presumed negligible in spicules and prominences.

The line width [$\Delta\lambda$] is related to the FWHM in the case of a Gaussian emission profile by

$$\Delta\lambda = \frac{\rm FWHM}{2\sqrt{\ln 2}} = \sqrt{2}\sigma, \tag{2}$$

where σ is the width of the Gaussian.

With line widths of two simultaneously observed spectral lines from two different chemical elements with different molecular weights [μ_i], we can derive an estimate for both the kinetic temperature and the velocity equivalent of the non-thermal line broadening. For $n > 2$ observed spectral lines, Equation (1) leads to a set of n equations for the two open parameters $T_{\rm kin}$ and $v_{\rm non\text{-}th}$ that can be solved by a matrix inversion or a least-squares fit.

The whole approach assumes emission profiles of Gaussian shape, *i.e.* without central reversals by self-absorption, and that the observed spectral lines have to form in the same solar atmospheric volume or at least under the same atmospheric conditions. With the variation of opacity from line to line in the chromosphere, the second condition is not automatically fulfilled even for features that appear to be on the same spatial location in the data (*e.g.* Stellmacher and Wiehr, 2015). The first condition can be estimated from the line shape.

We determined $T_{\rm kin}$ and $v_{\rm non\text{-}th}$ using Equations (1) and (2) for all pairs of lines and all lines together only for the data taken in 2011 because they could be aligned precisely thanks to their high spatial resolution. The width [σ] of the Gaussians that were fitted to the profiles was corrected beforehand for the instrumental broadening [$\sigma_{\rm instr}$] of the respective spectrograph (Tandberg-Hanssen, 1960, his Equation II.12). The value of $\sigma_{\rm instr}$ was determined by convolving the FTS atlas profiles with a Gaussian to match the line width of photospheric lines in the observed spectra (*cf.* Cabrera Solana *et al.*, 2007). The velocity equivalents of the instrumental broadenings were, however, only about 2 km s^{-1}, which is nearly negligible in comparison to $v_{\rm non\text{-}th}$. Therefore, this correction had only a small effect on the final values of $T_{\rm kin}$ and $v_{\rm non\text{-}th}$.

4. Results

4.1. 2D Spectroscopy in Hα

4.1.1. GFPI Data

Figure 2 shows one of the 39 scans through the Hα line taken with the GFPI (observation 6, setup 3). An animation of the complete time series is available as Electronic Supplementary Material (see spic_anim.mp4 and Puschmann, 2016a). Individual spicules can best be identified in the line-wing image, while in the line-core image the complete off-limb region shows a more diffuse emission pattern. In the maps of the FWHM from the Gaussian fit (top right panel of Figure 2), individual spicules show an increased FWHM relative to their

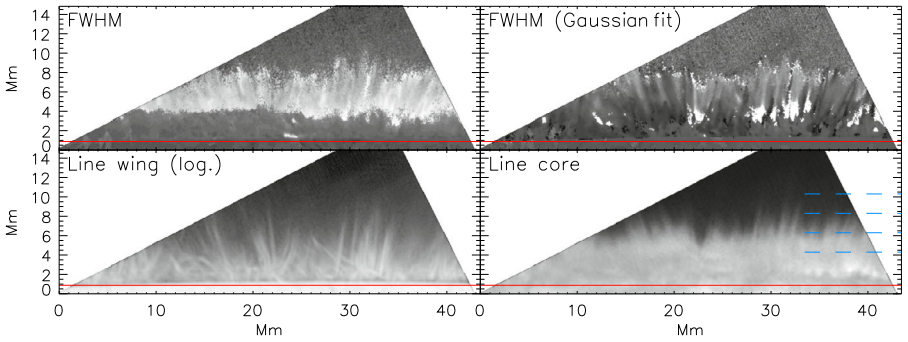

Figure 2 Example of the GFPI Hα observations at the limb (observation 6). Top row, left to right: FWHM from direct determination and FWHM from fit of a Gaussian. Bottom row, left to right: line-wing intensity in logarithmic display and line-core intensity. The red horizontal line marks the approximate location of the limb. The blue dashed lines in the lower-right panel indicate the heights above the limb of the spectra shown in Figure 5. An animation of the complete time series is available as Electronic Supplementary Materials (see spic_anim.mp4).

surroundings, but in most cases without any clear trend along their length (see also Pereira, Rouppe van der Voort, and Carlsson, 2016).

To trace the temporal evolution of the emission, we selected one prominent spicule within the time series (Figures 3 and 4). It can be clearly distinguished in the line-wing images at $t = 44$ s (left column in Figure 3, third panel from the bottom) and can be followed until $t = 396$ s. Its line width is larger than that of the surroundings (Figure 3, third and fourth column), but reduces with increasing limb distance in most cases. The spectra along the central axis of the spicule (Figure 4) resemble those from the TESOS data in Figure 7, but show larger Doppler shifts, especially toward the blue at the beginning (t in the range 88 – 220 s). The spicule expands up to a height of about 6 Mm at $t = 242$ s. The average spectra from all spatial locations and all of the 39 wavelength scans show a reduction of the line width with increasing limb distance (rightmost panel in Figure 4).

Because of the difficulties in extracting the line width from the GPFI spectra, we also selected individual spectra at different heights above the limb to follow their temporal evolution (Figure 5 and the animation provided as Electronic Supplementary Material, spic_anim.mp4). Figure 5 shows the temporal evolution of individual spectra at four of those heights above the limb. Like in the animation, the presence of large and varying Doppler shifts is clearly visible, but the disappearance of some bright emission is usually not connected to an increase in line width but only to a fading with time.

4.1.2. TESOS Data

Figure 6 shows line-core images in Hα taken with TESOS during observation 1 (*cf.* Table 2, setup 1). The cadence between subsequent images is about 30 s. The corresponding FOV in the other spectral lines is shown in Figure 10 below. In the top left panel of Figure 6, the approximate location of the TIP slit inside the TESOS FOV is indicated by a dash-dotted horizontal line. Each line-core image is displayed twice, with and without an unsharp masking that enhances small-scale features. The limb location was determined from the corresponding continuum intensity images (not shown) and was used to delineate the region in which the stray-light correction with the second correction method (see Section 3.1) was applied. Its approximate location shows up at about the middle of the FOV as a vertical line

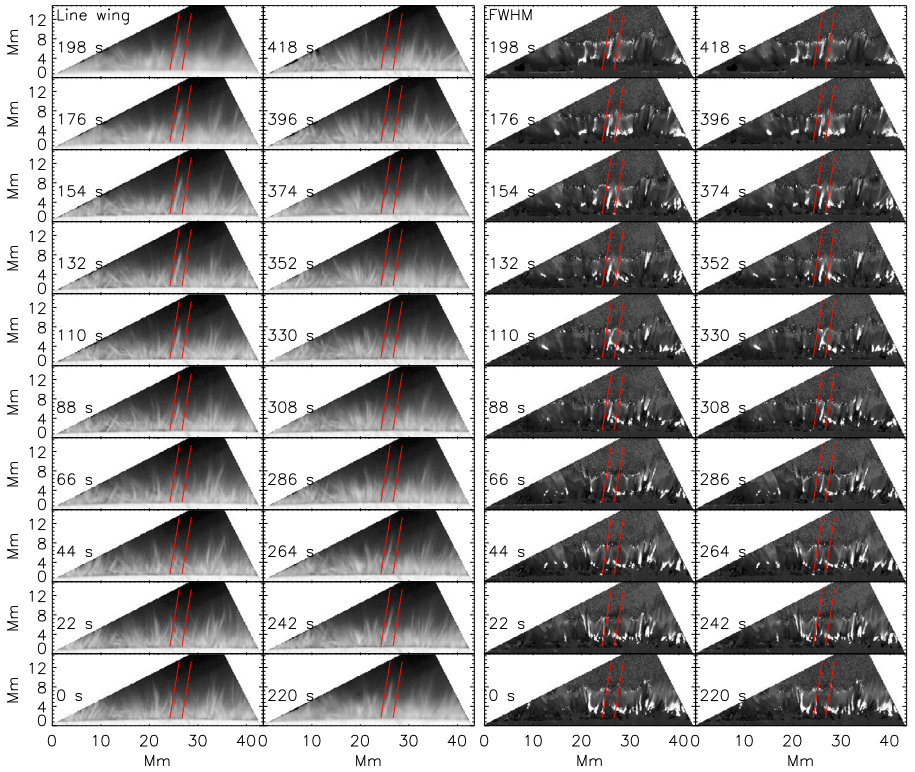

Figure 3 Evolution of an individual spicule in line-wing images (left panels) and in maps of the FWHM from a Gaussian fit (right panels) in the GFPI Hα data. The spicule is located between the two inclined red lines in each subpanel. It starts at about $t = 44$ s and has disappeared at $t = 396$ s. Time increases from bottom to top in each column in the corresponding panels. An animation of the complete time series is available as Electronic Supplementary Materials (see spic_anim.mp4).

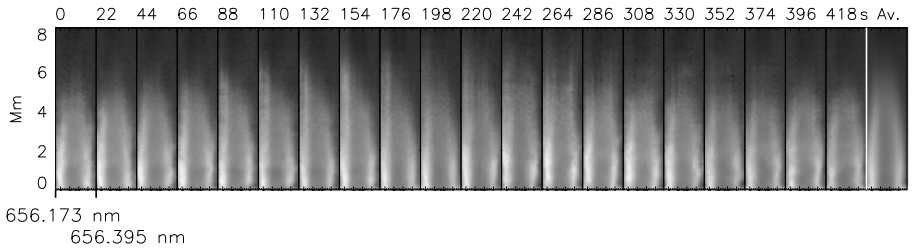

Figure 4 Individual spectra during the evolution of the spicule that is marked in Figure 3. The wavelength increases from left to right in each subpanel, within the range given at the leftmost subpanel. The rightmost panel shows the off-limb spectra in the GFPI data averaged over all 39 bursts and all spatial positions along the limb.

in each image. The FOV slowly drifts with time because of the cotemporal scanning of the slit-spectrograph instruments. To extract the spectral properties of individual spicules, we masked some intensity enhancements in the Hα line core above a height of about 5 Mm beyond the limb (white dash-dotted contours in the top panels of each row). We note that

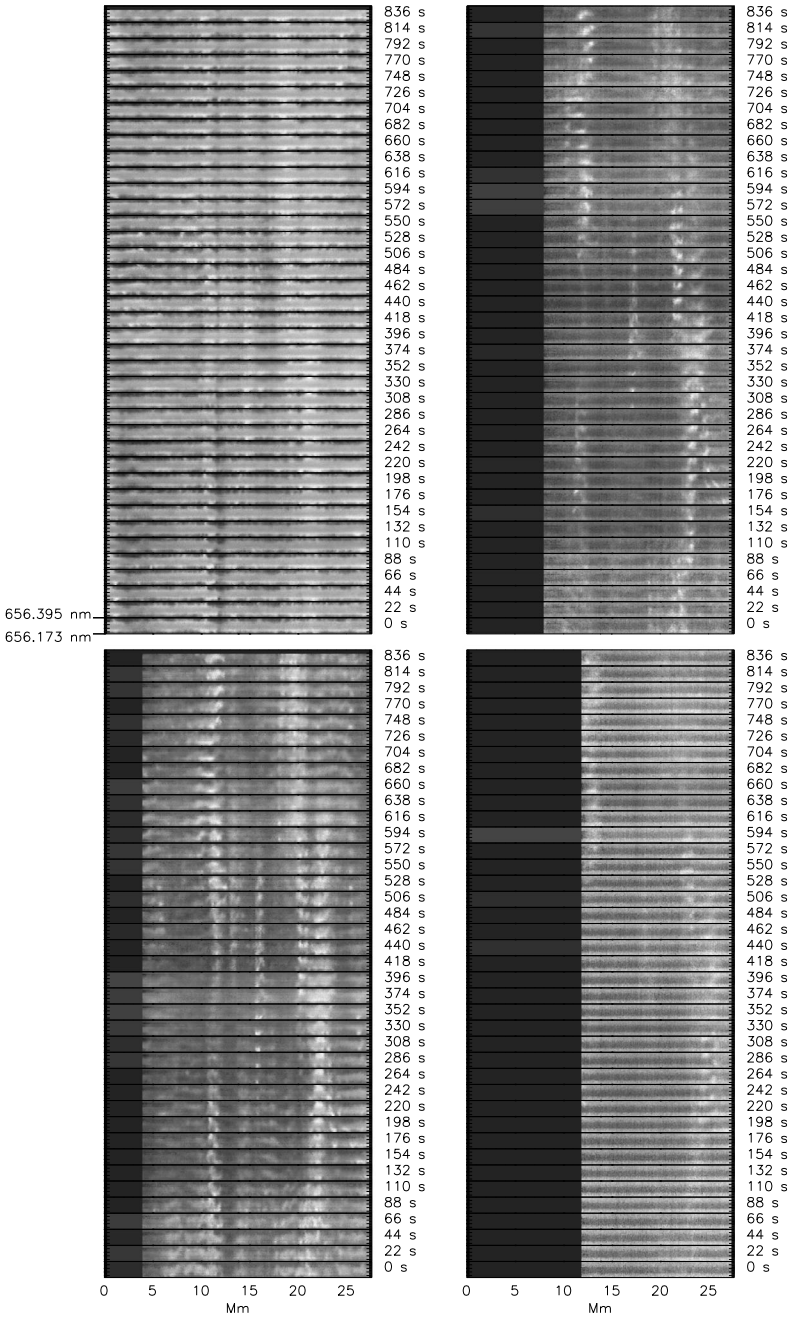

Figure 5 Temporal evolution of Hα spectra at different heights above the limb in the GFPI data. Left column: $h = 4.3$ Mm (top), $h = 6.3$ Mm (bottom). Right column: $h = 8.3$ Mm (top), $h = 10.3$ Mm (bottom). Time increases from bottom to top and the spatial position along the limb increases from left to right in each panel. The wavelength increases from bottom to top in each subpanel, within the range marked in the lower subpanel of the top left panel. An animation of the complete time series is available as Electronic Supplementary Materials (see spic_anim.mp4).

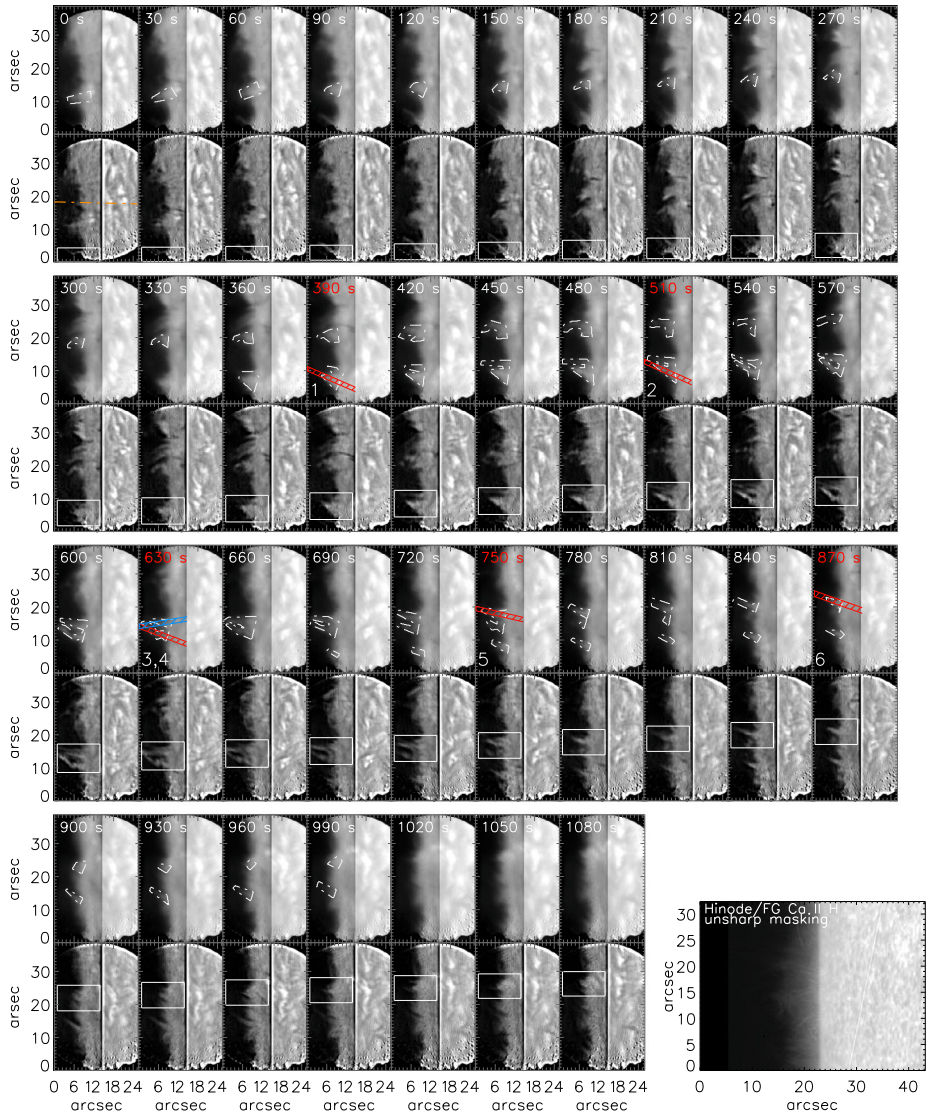

Figure 6 Hα line-core images acquired with TESOS during observation 1. Time increases from left to right and top to bottom. For each time step, the original (unsharp masked) line-core image is displayed in the upper (lower) panel. The white dash-dotted contour lines mark the area of some individual spicules. The white rectangles follow the location of one specific feature with time. The red and blue hatched areas (with corresponding time of observation given in red in the relevant subpanels) denote the range of averaging for the profiles 1 to 6 shown in Figure 7. The orange dash-dotted line at $t = 0$ s indicates the location of the TIP slit. The bottom rightmost panel shows a cutout from a broadband Ca II H image from *Hinode* for comparison.

below this height it is nearly impossible to reliably identify individual features in line-core images because different features completely overlap.

We selected one feature that was covered throughout its lifetime (*cf.* the white rectangles in Figure 6) to determine laterally averaged profiles along its extent at five different time

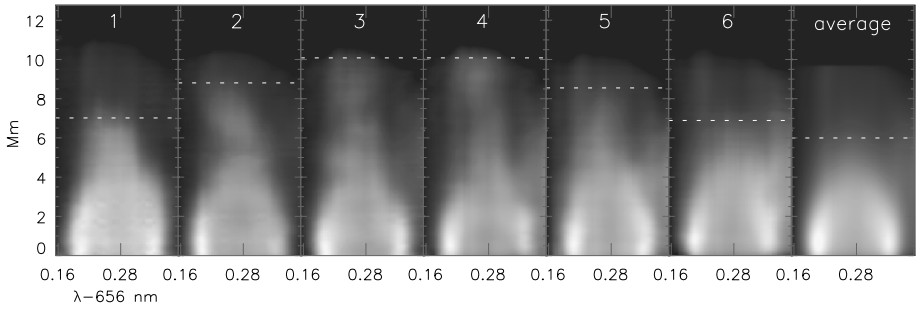

Figure 7 Average Hα profiles in one spicule feature. Left to right (panels labeled as 1 – 6): red hatched area of Figure 6 at $t = 390, 510, 630$ s, blue hatched area at $t = 630$ s, red hatched area at 750 and 870 s. The rightmost panel shows the average off-limb profiles. The horizontal white dotted lines denote the greatest height at which the spectra are still significant. The x-axis gives the wavelength of the spectra minus 656 nm.

steps (*cf.* the six blue and red hatched areas marked in Figure 6). The feature, or at least a predecessor of the feature at the same spatial location, can be identified already at $t =$ 60 s (third column in the top row at location $x, y \approx 8'', 3''$) when its evolution is followed backward in time. It rises over the course of ≈ 300 s to a greatest height of about $16''$ above the limb at $t = 630$ s. It retracts subsequently toward the limb and cannot be identified any longer at $t = 930$ s.

Figure 7 shows the spatially averaged line-profiles, *i.e.* those obtained averaging laterally along the y-axis of the images in Figure 6 over the colored hatched areas (labeled 1 to 6 in Figure 7) at the corresponding time step during the observations, with limb distance increasing along the vertical direction in the figure. The feature is roughly oriented (tilt of less than 30 degrees) perpendicular to the limb, so the laterally averaged profiles roughly sample its extent in height above the limb. The temporal variation of its greatest height (marked as a horizontal white dotted line in each panel of Figure 7) is roughly parabolic. The profiles all show a change from self-absorption with a central absorption core up to a height of about 2 Mm above the limb to pure emission profiles at higher layers. Visually, the line width constantly decreases with height. The same holds for the average off-limb profiles shown in the rightmost panel of Figure 7 that were retrieved by averaging over nearly the full extent of the FOV, excluding the top and bottom borders because of the curved field-stop. In the profiles averaged over the full usable FOV, only spectra up to about 6 Mm above the limb have intensities higher than the noise level, similar to the GFPI spectra in Figure 4. The profiles marked as 4 to 6 in Figure 7 exhibit a faint haze at the red end of the spectrum ($\lambda \approx 656.34$ nm), which is some flat-field residual that could not be corrected for.

The individual profiles along the two branches of the feature that have developed at $t = 630$ s (marked as red and blue hatched areas in the corresponding panel of Figure 6) are shown in Figure 8. The FWHM derived from the Gaussian fit and that derived directly using the locations where the intensity drops to 50 % of its maximum are overplotted with short red and blue bars, respectively. The FWHM is seen to decrease up to a height of about 5 Mm above the limb, and remains at best constant at higher layers. The corresponding FWHMs in all six sets of laterally averaged profiles are shown in Figure 9. Up to the height where the intensity in the spectra is still significant, all six examples of the height variation in the FWHM in resolved features show a monotonic decrease in width. The FWHM only increases just where the spectra level off into the noise (profile sets 1, 2, and 6 in Figure 9). The FWHM retrieved through Gaussian fitting agrees reasonably well for most spectra with that obtained using the direct method, which, however, apparently tends to give noisier results.

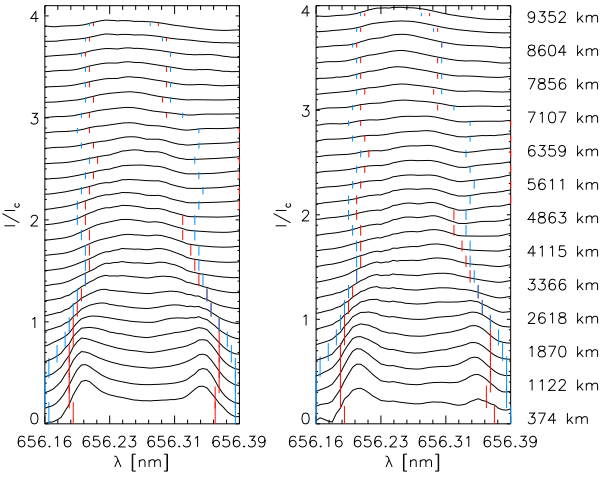

Figure 8 Individual profiles from the laterally averaged sets of spectra 3 (left) and 4 (right) of Figure 7. The profiles are displaced from each other in y for better visibility. The corresponding heights above the limb are given at the right-hand side. The blue and red bars denote the FWHM from a Gaussian fit and that derived directly using the locations where the intensity drops to 50 % of its maximum, respectively.

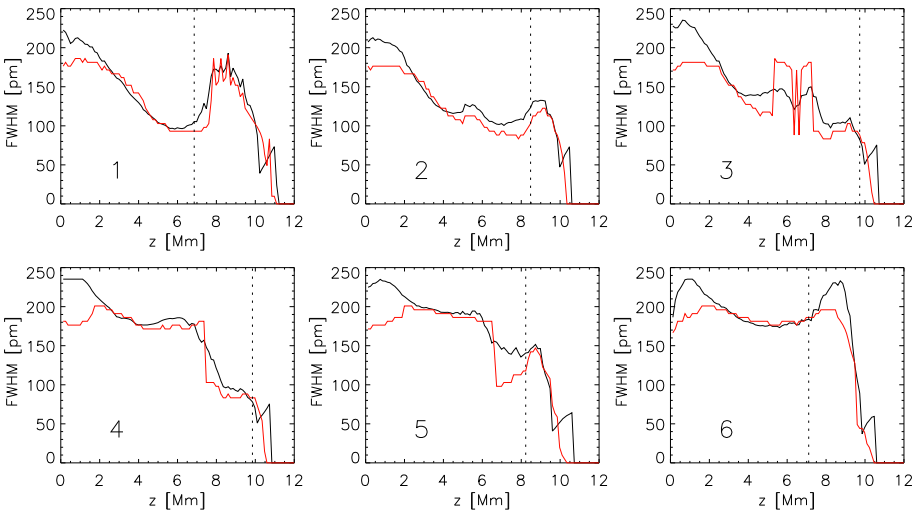

Figure 9 The FWHM of the same Hα profiles as in Figure 7. Black: FWHM of the Gaussian fit. Red: FWHM of the locations where the intensity drops to 50 % of the maximum. The vertical dotted lines denote the greatest height at which the spectra are still significant.

This might be related to the fact that the Gaussian fit makes use of all wavelength points in the line profile, whereas the direct method is only based on three wavelength points, *i.e.* the one corresponding to the highest intensity and the two locations for which the line profile reaches a level of 50 % of that value. The latter method is therefore more sensitive to noise peaks.

Other examples of time series of Hα line-core images are shown in Figures 21 – 24. They all share more prominently than Figure 6 a certain peculiarity, which, however, is also apparent in the latter: the majority of the individual structures or features that are seen above a limiting height of about 5 to 6 Mm show little to no resemblance to spicules, *i.e.* only a very few features are elongated, slender brightenings jutting out and away from the limb. Figures 21 and 22 clearly show material, or more precisely, brightenings that recede from

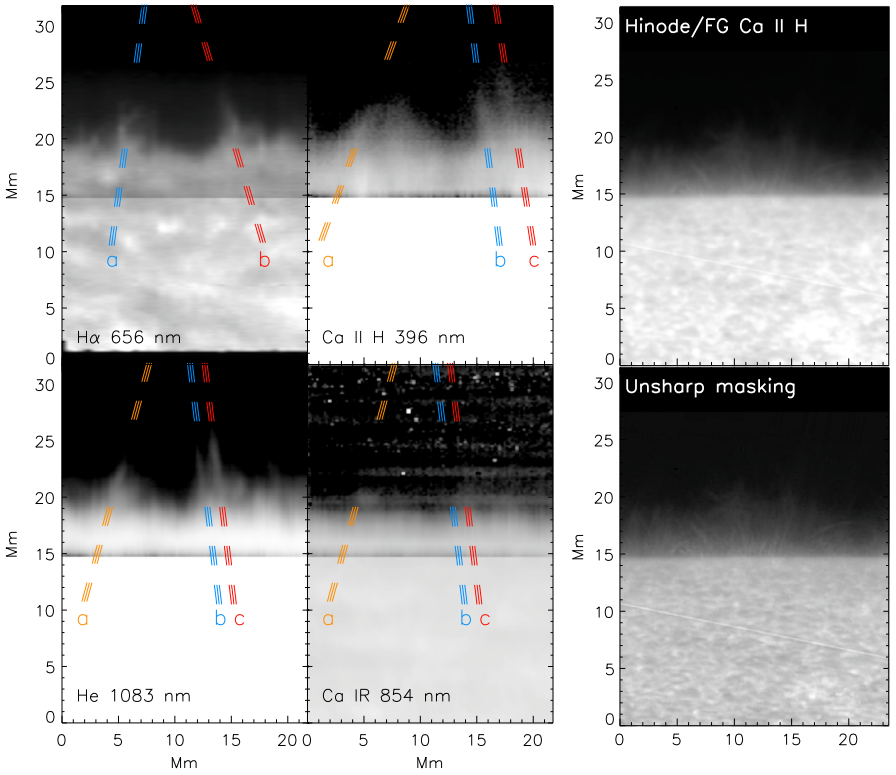

Figure 10 Left: FOV of observation 1 in line-core images of different spectral lines. Clockwise, starting with the left top: artificial Hα scan, Ca II H, Ca II IR at 854.2 nm, and He I at 1083 nm. The inclined colored lines labeled a, b, and c denote the regions over which the profiles shown in Figure 11 were laterally averaged. The two panels at the right-hand side show an equal-sized region from a broadband Ca II H image from *Hinode* without (top) and with an unsharp masking (bottom) for comparison.

the limb upwards (bottom rows of both figures), but the corresponding shapes are either elongated structures that are parallel to the limb, or roundish blobs. The same holds for Figure 23, only complex-shaped features appear at heights of more than about 6 Mm above the limb in the Hα line-core images.

4.2. Slit-Spectrograph Data

The left four panels of Figure 10 show the corresponding FOV of observation 1 in the slit-spectrograph data. We constructed a pseudo-scan map (*e.g.* Beck *et al.*, 2007) of the same FOV from the 2D Hα spectra from TESOS. We selected the TESOS wavelength scan closest in time to each scan step of the slit-spectrograph instruments for that purpose and cut out the corresponding spectra along the location of the TIP slit from the TESOS 2D FOV (top left panel of Figure 6). The resulting map (upper left subpanel of Figure 10) shows how the temporal evolution of Figure 6 is sampled in a slit-spectrograph observation. A prominent change is that most of the laterally extended structures in the 2D Hα line-core images appear as a series of resolved, rather thin and elongated features in the pseudo-scan map. We did not try to improve the spatial alignment because all other spectra in the different wave-

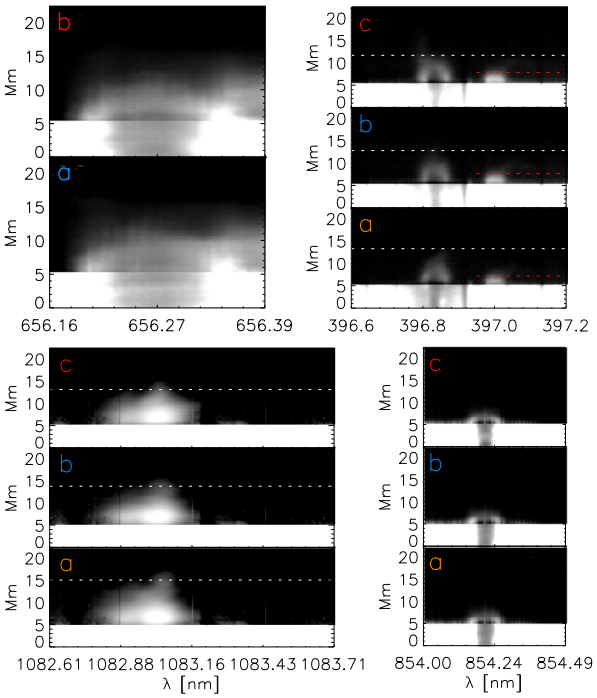

Figure 11 Laterally averaged spectra along the colored lines labeled a, b, and c in Figure 10. Clockwise, starting left top: Hα, Ca II H, Ca II IR at 854.2 nm, and He I at 1083 nm. The horizontal dotted lines denote the greatest height with spectra above the noise level.

length ranges are not strictly cospatial and simultaneous as a result of the large differential refraction at the early time of this observation and the sequential scanning.

The line-core images in Hα, Ca II H, and He I at 1083 nm are to some extent similar, showing one set of spicular features at $x \approx 5$ Mm, a region of reduced extent of emission from x between 7 and 12 Mm, and a double pair of spicules at $x \approx 14$ Mm. These three lines therefore probably form in a similar volume, *i.e.* their optical depth should be comparable and they should sample the same atmospheric volume. The line-core image of Ca II IR at 854.2 nm differs significantly from all others. The extent of emission is limited to about 5 Mm above the limb and very few or no isolated features can be identified. The two panels at the right-hand side of Figure 10 show a similar-sized region from a broadband Ca II H image from the *Hinode* filtergraph for comparison. For the bottom panel, the image was treated with an unsharp masking to enhance the contrast. The *Hinode* Ca image shows that the apparently uniform emission from the limb to about 5 Mm height above it in the line-core images is composed of individual strands of spicules. The only clear examples of isolated, individual spicules in the spectra (*cf.* the inclined colored lines) are found at heights where the *Hinode* Ca image exhibits little to no emission any longer.

To quantify the properties of the three (two in Hα) spicules in the different spectral lines, we again averaged the spectra laterally, *i.e.* along the x-axis, over the extent of the inclined colored lines in Figure 10. As before, the spicules are nearly perpendicular to the limb, so that the variation with limb distance simultaneously samples the variation along the spicule length. The corresponding sets of profiles are shown in Figure 11. All spectra are displayed on a logarithmic intensity scale to enhance the visibility of their shapes. The profile shape and its variation with height for Hα and the Ca II H and IR lines is similar. The spectra show a self-absorption core close to the limb that changes to a single central emission, and a decrease in line width with height (see also Pasachoff, 1970; Pasachoff and Zirin, 1971). For

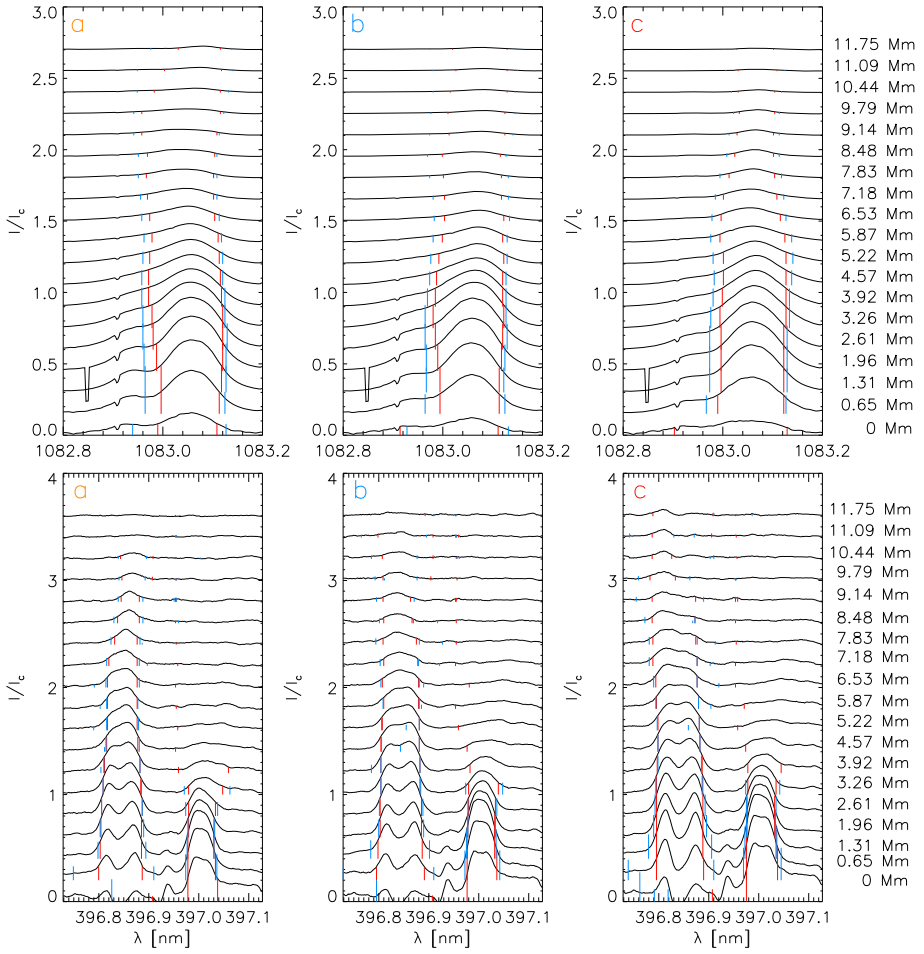

Figure 12 Laterally averaged spectra along the colored lines labeled a, b, and c in Figure 10. Top row: He I at 1083 nm. Bottom row: Ca II H and Hε. The blue and red bars denote the FWHM from a Gaussian fit and that derived directly using the locations where the intensity drops to 50 % of the maximum, respectively.

Ca II IR at 854.2 nm, the height scale of this variation is compressed by about two compared to the other lines. The Hε line to the red of the Ca II H line core at 397 nm shows emission to about the same height as Ca II IR at 854.2 nm. The amplitude of the emission in Hε exceeds the one of Ca II H close to the limb. The shape of the He I line at 1083 nm is different from all others because of its specific formation and because it is made of several components (*e.g.* Sánchez-Andrade Nuño *et al.*, 2007), but it shows a similar trend of a reduction in line width with height.

The individual spectra of Ca II H and He I at 1083 nm for the three chosen spicules are shown in Figure 12. For He I at 1083 nm, the line width increases up to a height of about 6 Mm, but this broadening is artificial and caused by the merging of the red and blue components of the lines. The line width decreases at larger heights. For the Ca II H spectra, the line width reduces only slightly up to about 7 to 8 Mm in all panels, but above this height, the emission peak becomes significantly smaller. Hε shows a different behavior, with

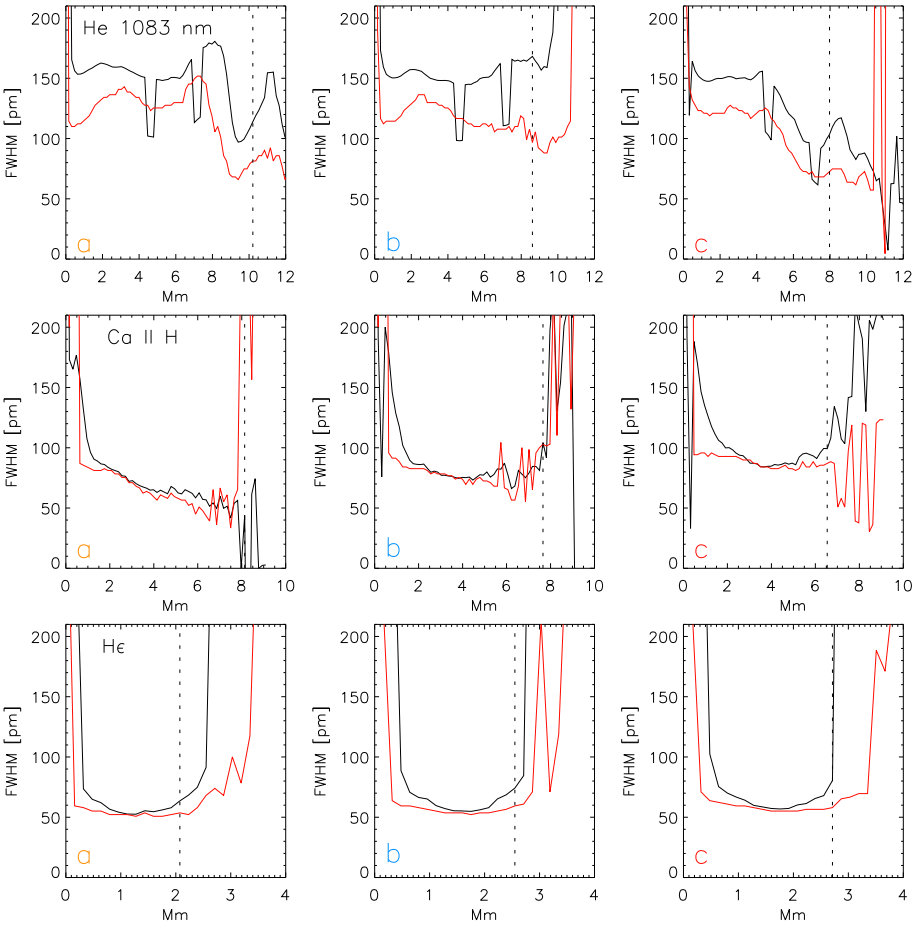

Figure 13 The FWHM of the laterally averaged spectra along the colored lines labeled a, b, and c in Figure 10. Black: FWHM from the Gaussian fit. Red: FWHM from the locations where the intensity drops to 50 % of the maximum. The vertical dotted lines denote the [maximal height] range with spectra above the noise level as marked in Figure 11.

a broadening of the line at about 3 Mm, but at the same time the intensity of the emission is already nearly zero. The spectral line seen in emission between Ca II H and Hε up to a height of nearly 2 Mm should pertain to singly ionized iron (*cf.* Engvold and Halvorsen, 1973; Lites, 1974; Rutten and Stencel, 1980; Watanabe and Steenbock, 1986; Schmidt and Fisher, 2013).

Figure 13 shows the FWHM of the laterally averaged profiles for He I at 1083 nm, Ca II H, and Hε. Except for Hε, the general trend is a decrease in line width with height. For Hε, the line width increases in all three locations about 0.5 Mm in height before the emission has vanished completely. We note that this apparent increase in line width in Hε occurs at about 2 – 3 Mm, where all other lines indicate a usually monotic decrease in line width.

Figure 14 shows all parameters retrieved from the Gaussian fit for the He I, Ca II H, and Hα spectra throughout the full FOV of observation 1 as a cross-check of the behavior

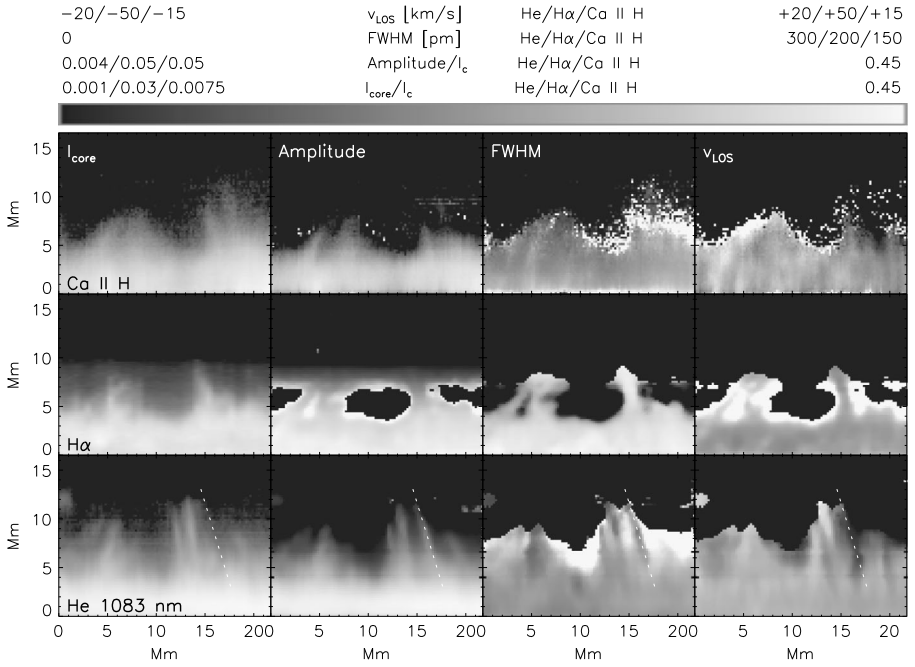

Figure 14 Results of the Gaussian fit for observation 1. Left to right: line-core intensity, amplitude, FWHM, and LOS velocity of the fitted Gaussian. Top to bottom: Ca II H, Hα, and He I at 1083 nm. The white inclined dotted line in the bottom row marks a region of reduced FWHM in He I at 1083 nm. The solar limb is at $y = 0$ Mm. The gray bar at the top gives the display ranges for the respective parameters and lines. The lowest (at the left) and highest (at the right) values are given from left to right for He I at 1083 nm, Hα, and Ca II H, and from top to bottom for the LOS velocity, FWHM, emission amplitude, and line-core intensity, respectively.

of the line width in individual spicules. Only the off-disk area of the FOV is shown. The line width in Ca II H shows a faint lateral structuring (*e.g.*, at $x \approx 4$ to 8 Mm), but no clear vertical variation. At best a weak trend for a reduction of the FWHM with height can be discerned. In Hα, the features at $x \approx 5$ and 15 Mm show an increase in the FWHM at the upper ends, but the intensity at these places is already low. Appendix B shows in more detail that and why the values derived from these profiles are spurious, whereas the Gaussian fit works acceptably well for profiles closer to the limb. In He I, one out of the five distinct features that can be identified (two at $x \approx 5$ Mm, three at 15 Mm) shows an increase in the FWHM at the upper tip similar to those seen in Hα. The FWHM increases up to the display threshold limit at the greatest height for which values are shown in each column, but a comparison with the line-core intensity or the amplitude of the Gaussian reveals that these values are spurious because the intensity is nearly zero at these locations (*cf.* between $x \approx 7$ to 11 Mm: the large FWHM (white) at $y \approx 7$ to 9 Mm coincides with nearly zero amplitude of the Gaussian). The FWHM and the LOS velocities in He I show similar patterns with more lateral fine-structure than the line-core image. The patterns of low/high FWHM or positive/negative LOS velocity are oriented similar to the spicules in the line-core images, with the same tilt relative to the limb and the same vertical extent. No clear relation between the FWHM and the LOS velocities can, however, be derived because all combinations of positive or negative LOS velocities with low or high FWHM can be found. The

same holds for any possible relation of either FWHM or LOS velocities with high or low intensity.

Observations 2 – 4 are displayed in Appendix C. They yield the same result as obtained from observation 1, the line width decreases with increasing limb distance up to the point where the spectra show no significant emission any longer.

The spatial resolution of all of the slit-spectrograph data shown up to here was partially impeded by the limited performance of the AO system that had to operate with a facula as the main feature for the correlation. A comparison of the previous figures of the slit-spectrograph data with Figure 15 immediately shows the advantage of a better-suited AO lock point such as a sunspot. Except for the top row of Figure 15, the images were constructed from the reduced and calibrated spectra with no additional treatment but the stray-light correction. These data, however, now correspond to an active region instead of the quiet Sun. The bottom row of Figure 15 shows the continuum intensity in the full FOV in He I at 1083 nm, Ca II IR at 854.2 nm, Hα, and Ca II H to facilitate control of the spatial alignment. We used the sunspot inside the red rectangle for this purpose. Because the differential refraction was again very strong early in the morning when the corresponding observations were taken, the Ca II H data are less well aligned than all others, even if it is not obvious in the image. Features in the Ca II H images are at the same place after the alignment, but the corresponding Ca II H spectra were taken about 70 (100) s earlier than those of Hα (He I).

The line-core images of Figure 15 show several resolved spicules and macrospicules of up to 20 Mm extent at the limb. No relation of the off-limb structure to the sunspot on the disk is directly obvious, *e.g.*, by connecting intensity brightenings or darkenings. The red rectangles in the second row from the bottom outline a cluster of spicules. Their appearance changes significantly between the different spectral lines, with both the Ca II H and the IR line showing individual strands instead of the more uniform structure seen in Hα or He I at 1083 nm. The time difference between the Ca II IR and Hα (He I) is zero (30 s), so the different appearance in these three lines is probably not caused by the temporal evolution. The largest macrospicule at $x \approx 5$ Mm exhibits a substructure of a dark central core in the He I line-core image, whereas the corresponding bright feature in Ca II IR at 854.2 nm seems to correspond only to the central part of the macrospicule.

Figure 16 shows the results of applying the Gaussian fit to the spectra of observation 5. Only the off-limb region of the FOV is shown. We did not filter out the pixels without significant emission, where the results of the Gaussian fit are only spurious, as in all previous figures, because in all spectral lines the transition into noise can be clearly identified in one or all of the Gaussian parameters, usually best in the FWHM and LOS velocity. The FWHM in the cluster of spicules at $x \approx 15$ to 20 Mm is similar for Hα, Ca II IR at 854.2 nm, and He I at 1083 nm, but shows a much stronger lateral structuring with an iterative change from low to high FWHM in Ca II H. In all lines, the FWHM decreases or remains at best constant with height above the limb for the cluster of spicules. In the largest macrospicule at $x \approx 5$ Mm, the central axis shows an increased FWHM in all lines and a reduction at the tip of the structure in all lines but Ca II IR at 854.2 nm.

We applied Equations (1) and (2) to the roughly simultaneous, cospatial spectra of observation 5 to obtain an estimate of the kinetic temperature and the non-thermal line width (Figure 17). We used all line pairs of different chemical elements and a least-squares fit to all lines simultaneously (rightmost column). The different line pairs give rise to slightly different results, but some characteristics are common. The kinetic temperature in the cluster of spicules at $x \approx 18$ Mm ($< 30\,000$ K) is lower than in the macrospicule at $x \approx 5$ Mm (up to above 50 000 K). The temperature is generally lower toward the upper end of both structures. A similar reduction in kinetic temperature with height is to first order also seen in

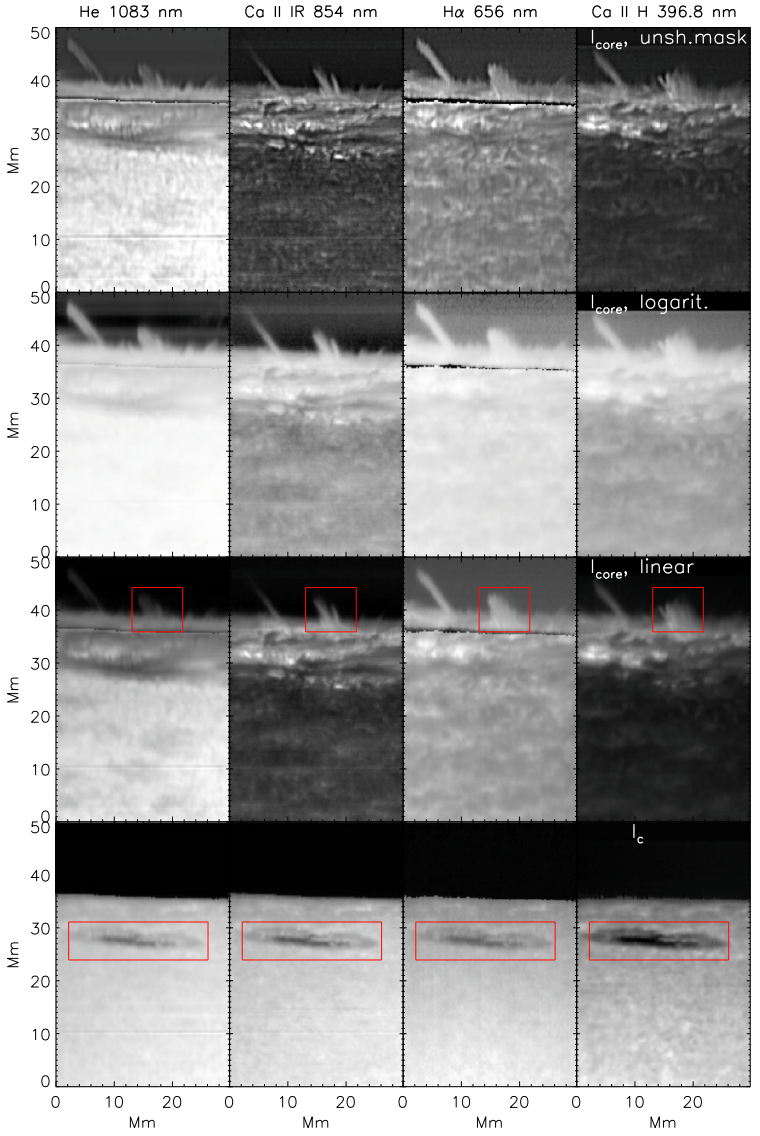

Figure 15 Overview of the FOV of observation 5 taken on 12 April 2011. Left to right: He I at 1083 nm, Ca II IR at 854.2 nm, Hα, and Ca II H. Bottom to top: continuum intensity, line-core intensity in linear display, the same in logarithmic display, and the same with unsharp masking. The red rectangles outline some features in the FOV that highlight the accuracy of the spatial alignment (bottom row) and the different appearance in the line core of different spectral lines (second row from the bottom).

the remaining FOV, especially from the layers close to the limb ($y < 5$ Mm) toward higher layers. The non-thermal line width slightly increases at the top of the macrospicule when the Ca II IR spectra are involved, whereas for all other line pairs and combinations it decreases. The non-thermal line width is about 5 to 10 km s^{-1} in the cluster of spicules and above 15 km s^{-1} in the isolated macrospicule. Across the FOV, the non-thermal line width

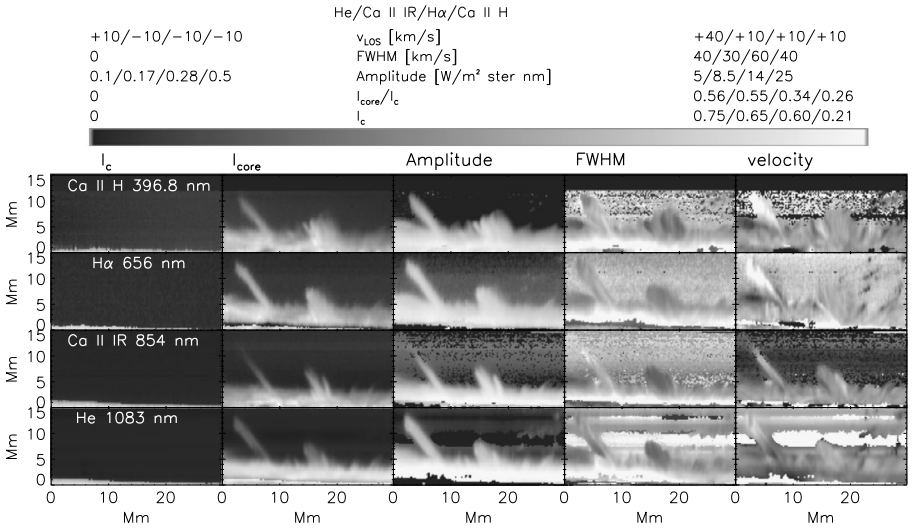

Figure 16 Results of the Gaussian fit for observation 5. Left to right: continuum intensity, line-core intensity, amplitude, FWHM, and LOS velocity. Top to bottom: Ca II H, Hα, Ca II IR at 854.2 nm, and He I at 1083 nm. The gray bar at the top gives the display ranges for the respective parameters and lines. The lowest (at the left) and highest (at the right) values are given from left to right for He I at 1083 nm, Ca II IR, Hα, and Ca II H, and from top to bottom for the LOS velocity, FWHM, emission amplitude, line-core intensity, and continuum intensity, respectively.

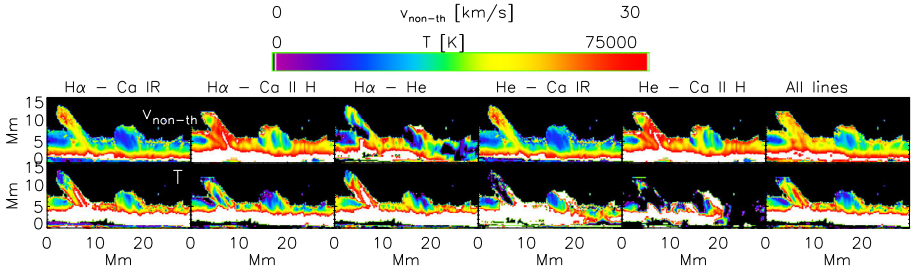

Figure 17 Kinetic temperature [$T_{\rm kin}$] (bottom row) and non-thermal velocity [$v_{\rm non\text{-}th}$] (top row). Left to right: $T_{\rm kin}$ and $v_{\rm non\text{-}th}$ from the line pairs Hα – Ca II IR, Hα – Ca II H, Hα – He I, He I – Ca II IR, He I – Ca II H, and the fit to all lines together.

decreases with height similar to the kinetic temperature, with a sharp drop at a height of about 5 Mm.

4.3. Average Off-Limb Spectra

Figures 18 and 19 show the average off-limb spectra in Ca II H, Hα, Ca II IR at 854.2 nm, and He I at 1083 nm for observations 1 and 5, respectively. The Hα spectra in Figure 18 were taken with TESOS and therefore cover only a small wavelength range around the line core, whereas the Ca II H spectra were recorded with the PCO inside of POLIS and also include the Hε line. In Figure 19, the Hα spectra were recorded with a PCO and cover the full prefilter curve, whereas the Hε line was not covered in the Ca II H spectra because we

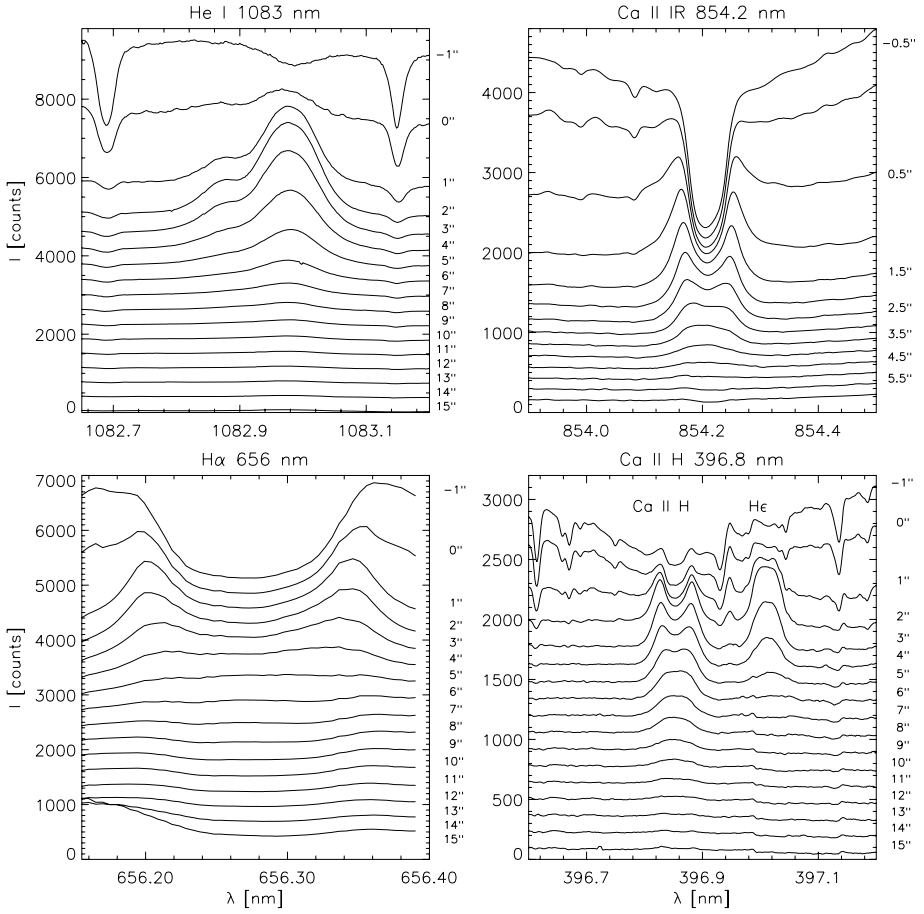

Figure 18 Average off-limb spectra of observation 1 (*cf.* Figure 10) of (clockwise, starting left top) He I 1083 nm, Ca II IR 854 nm, Ca II H, and Hα. The location of the profiles relative to the limb is given at the right-hand side of each panel. Subsequent profiles are offset in y for better visibility. For Ca II IR at 854.2 nm, only profiles up to a height of 6″ are shown.

used the default POLIS Ca CCD camera. The displayed wavelength range was clipped to the line-core region in all plots.

All plots of both observations show the same general trend in line width with increasing limb distance in all of the lines, *i.e.* the amplitude of the emission decreases strongly, causing some of them to virtually disappear at a height of 5 Mm, and the line width decreases up to the point where the amplitude is close to the significance limit, throwing doubt on the increase in line width at the uppermost heights because of the presence of some residual stray light (*cf.* the photospheric lines in the wings of Ca and Hα). The height range where the spectra are not significant is marked in red in the top panels and by a dotted vertical line in the bottom panels of Figure 19, respectively. Profiles in blue show either self-absorption or are flat-topped, which indicates line formation in an optically thick atmosphere (see Section 6.1 below).

For the data with the higher spatial resolution (observation 5 taken in 2011), we applied the Gaussian fit to the average profiles. The panels in the bottom row of Figure 19 show

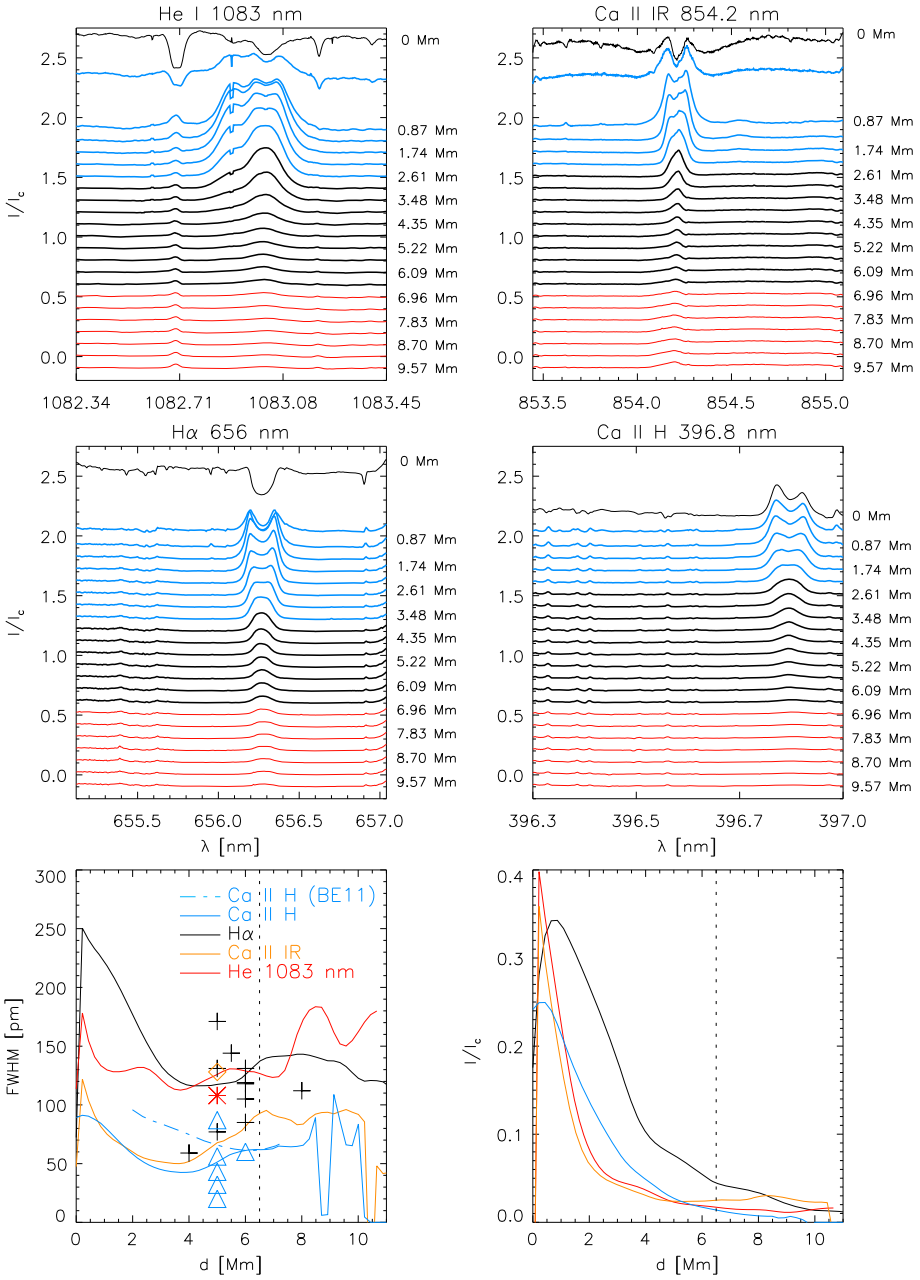

Figure 19 Top four panels: average off-limb spectra of observation 5 (*cf.* Figure 15) of (clockwise, starting left top) He I 1083 nm, Ca II IR 854 nm, Ca II H, and Hα. The location of the profiles relative to the limb is given at the right-hand side of each panel. Profiles in blue show self-absorption or are flat-topped. Profiles in red are considered to represent spurious intensities. Bottom panels: FWHM (left) and amplitude (right) of the Gaussian fit for the average spectra. The red asterisk, orange diamond, blue triangles, and black crosses denote the FWHM values of He I 1083 nm, Ca II IR 854 nm, Ca II H, and Hα given in Beckers (1968, 1972) and Alissandrakis (1973). The dash-dotted line marked as (BE11) indicates the results of Beck and Rezaei (2011).

the amplitude and the FWHM of the Gaussian for these average spectra. We extracted the line widths of the various lines from Beckers (1968, 1972) and Alissandrakis (1973) for comparison (small symbols in the lower left panel of Figure 19). These values show a quite significant scatter that usually covers our results for the respective lines, where our data have the advantage of a reliable limb distance and a complete coverage of the height range up to 10 Mm above the limb. From the values in the literature (Beckers, 1968, 1972; Alissandrakis, 1973), no clear trend in line width with height can be discerned. That the large scatter is a real problem caused by the use of different observations, recorded at different seeing conditions in different regions on the Sun can be seen by comparing the line width of Ca II H with the one determined for the same line in Beck and Rezaei (2011, dash-dotted line in the left bottom panel of Figure 19 marked as (BE11)). Using the same instrument and wavelength region, the line width retrieved by Beck and Rezaei (2011) is larger than for observation 5 up to a height of about 6 Mm. This might be caused by either the difference between active region or quiet-Sun off-limb features, or the difference in seeing with its related spatial smearing of structures at different Doppler shifts that affects the line width.

5. Summary

We have analyzed a set of multiwavelength spectroscopic observations at the solar limb in some of the strongest chromospheric spectral lines (Ca II H at 396.85 nm, Hε, Hα, Ca II IR at 854.2 nm, and He I at 1083 nm). The setups used at the German VTT to obtain simultaneous spectra in all the lines were typically complex because several instruments with additional cameras were used to cover more spectral lines.

We analyzed the observed spectra considering two main points, *i.e.* the spatial structuring of the off-limb features and the line width of the spectral lines as a function of their limb distance in individual spicules, across the FOV, and in average profiles. A comparison of 2D spectroscopy in Hα with slit-spectrograph data in the other lines revealed that only Hα and He I at 1083 nm show significant emission above a height of about 5 to 6 Mm above the solar limb. Many of the structures seen in Hα above this height differ from the thin, elongated spicules seen closer to the limb, *i.e.* they have lateral widths of up to a few Mm and typically show complex shapes. In observations at our spatial resolution of about 1″, except for the GFPI data with a spatial resolution of about 0.″3, limb spicules merge into a dense forest without individual structure in line-core images up to a height of about 6 Mm, whereas in the Doppler velocity some spicules can still be identified at lower heights. Spicules extending above a height of 6 Mm can be seen as isolated, individual features. The lateral structuring is more pronounced than the vertical structuring, with some features maintaining their small lateral width of 1 Mm or less over a length of several Mm. Large-scale structures in Hα exhibit brightenings that propagate upward, mostly in the form of roundish blobs. These features typically appear only in connection with large-scale, complex-shaped structures that extend beyond the typical height range of spicules.

The line width in individual spicules decreases with height above the limb in most cases. Some lines maintain a roughly constant line width over a height range of a few Mm. We find an increase in the line width at the uppermost tips of spicules, but its significance is doubtful because the corresponding amplitude of the emission is at the noise level of the spectra. Our results for the line width in spicules are covered by values published in previous articles, but both the published values and our own measurements at two different times show a large scatter.

The derivation of kinetic temperatures and non-thermal velocities from the set of the best simultaneous spectra yields temperatures of about 10 000 to 70 000 K for spicules and macrospicules, respectively. The non-thermal velocities are between 10 and 30 $\mathrm{km\,s^{-1}}$. These values refer to off-limb structures seen near or in an active region, however. For our quiet-Sun data, we have no equivalent set of co-spatial and simultaneous spectra because of a significant temporal shift between different wavelengths caused by the combination of differential refraction and sequential scanning. The main reason for this drawback is that the POLIS slit could not be rotated to orient it perpendicular to the horizon, while additionally the location of POLIS in the observing room of the VTT caused the largest differential refraction effects early in the morning (*cf.* Appendix A of Beck *et al.*, 2007).

6. Discussion

For observations of individual spicules, a high spatial resolution is required. Figures 10 and 15 demonstrate that thanks to adaptive optics, ground-based spectrograph data with an integration time of a few seconds can achieve this. The pseudo-scan map of Hα in Figure 10 additionally proves that the slit-spectrograph data correspond to a correct sampling of the temporal evolution seen in the simultaneous 2D spectroscopic data, with the limitation for their interpretation that they only cut out a single position from a temporally fast evolving 2D pattern. To preserve the spectral information, *i.e.* the shape of the emission and any eventual Doppler shifts, it is necessary to integrate over a few seconds because of the low light level of down to a few percent of the disk-center intensity. Broadband filter observations do not maintain the spectral information, but allow us to use shorter exposure or integration times. They provide the option of studying the temporal evolution in detail (*e.g.* Pereira, De Pontieu, and Carlsson, 2012), but do not allow us to extract physical properties of the solar atmosphere from the data themselves, making the review of Beckers (1968), which summarizes results of data taken before, still the reference for the physical properties of spicules.

The extraction of physical properties also depends to some extent on the availability of multiple spectral lines. The distinction between thermal and non-thermal line width, or any more detailed modeling and analysis, requires more information than a single spectral line typically provides, with the exception of the He I line at 1083 nm that in itself has several components (Sánchez-Andrade Nuño *et al.*, 2007; Centeno, Trujillo Bueno, and Asensio Ramos, 2010; Martínez González *et al.*, 2012). Such multiwavelength capabilities are therefore important to preserve and provide in future solar-telescope projects such as the *Daniel K. Inouye Solar Telescope* (DKIST: Rimmele *et al.*, 2010) or the *European Solar Telescope* (EST: Collados *et al.*, 2010). It seems that in the past few decades similar multiwavelength data have mainly been recorded for prominences (far) off the solar limb (*e.g.* Stellmacher and Wiehr, 1981; Bendlin, Wiehr, and Stellmacher, 1988; Stellmacher, Wiehr, and Dammasch, 2003), but not for structures near and at the limb (except for Socas-Navarro and Elmore, 2005).

Stray light off the limb is a problem that needs to be dealt with in spicule observations. When no direct measurements of the point-spread function are available (*cf.* Beck, Rezaei, and Fabbian, 2011; Löfdahl and Scharmer, 2012), a wavelength region in the continuum, where off the limb no solar emission is expected, can be used for the stray-light correction. For off-limb observations in chromospheric lines with 2D spectrometers such as TESOS, IBIS, CRISP, or the GFPI, such a continuum wavelength point can be added to the spectral

observation sequence to precisely determine the limb location and to correct for the off-limb stray light.

We found a limited extent of about 5 to 6 Mm above the limb for spicules, if they are defined as elongated, thin intensity streaks. Only a few isolated spicules can reach up to a height of 10 Mm. Most other features seen above 6 Mm are complex, large-scale structures with a significant lateral extent of a few Mm. There are no clear indications for any increase in line width at the tip of spicules, neither in individual spicules nor on average in the spectral lines used in our study (Ca II H, Hε, Hα, Ca II IR at 854.2 nm, He I at 1083 nm). The same general decrease of line width in average spectra is also seen in Mg II spectra obtained with IRIS (Pereira *et al.*, 2014, their Figure 4). Structures above a height of 6 Mm do not exhibit a significantly larger line width than is seen below that height.

In our analysis of the line width, we did not try to distinguish between different types of spicular structures. This would have been possible only in the Hα time series from TESOS or the GFPI. One additional reason is that the distinction between the two types is still under debate (Zhang *et al.*, 2012; Skogsrud *et al.*, 2015). If the type II spicules are dominant in quiet-Sun regions, then they should also have an effect on average profiles or show up prominently across the field of view (*e.g.*, Figure 3).

6.1. Limitations of the Present Analysis

Our analysis has a few limitations for technical reasons and because of the intrinsic properties of the spectral lines observed. The low light level off the limb, which even reaches zero, introduces significant noise in the spectra. In addition, the stray light off the limb cannot be fully corrected for. The automatic analysis using a single Gaussian partly fails at emission amplitudes below 5 % of I_c (Appendix B). However, the most stringent limitation is that all of the lines form in an optically thick regime in the lower part of the atmosphere. A clear indication for this is the appearance of self-absorption or flat-topped profiles (Figure 19) because in the optically thin regime a Gaussian or Voigt profile shape should prevail. For the strong chromospheric lines (all but H_ϵ), the profiles indicate an optically thick regime up to a height of about 3 Mm above the limb. Our estimates of the line width, regardless of whether by the direct method or the Gaussian fit, overestimate the line width in the height range of optically thick line formation because the true highest emission amplitude cannot be determined. We manually fit single Gaussians to a few profiles with clear self-absorption by forcing the amplitude of the Gaussian to be larger than the observed peak emission values and adjusting the width by hand. This yielded a line width smaller by 20 % (8 %) at a height of 2.6 Mm (3.6 Mm) above the limb than for the automated single-Gaussian fit. The general decrease in line width with height above the limb was maintained, although with a smaller slope. The best way to avoid the influence of the line formation on the derivation of line width, which is interpreted as reflecting temperature, would be a full non-local thermodynamic equilibrium modeling of spicules at different temperatures and subsequent profile synthesis as done in Judge and Carlsson (2010, *e.g.*, their Figure 3), but for all lines of our observations. The interpretation of line width as temperature measure or the derivation of a kinetic temperature from the width of lines from different chemical elements comes with some uncertainty (Stellmacher and Wiehr, 2015).

6.2. Comparison to Rapid Blue Events

How can our finding of a decrease in line width with height above the limb be reconciled with that of Rouppe van der Voort *et al.* (2009), who reported that rapid blue events (RBEs),

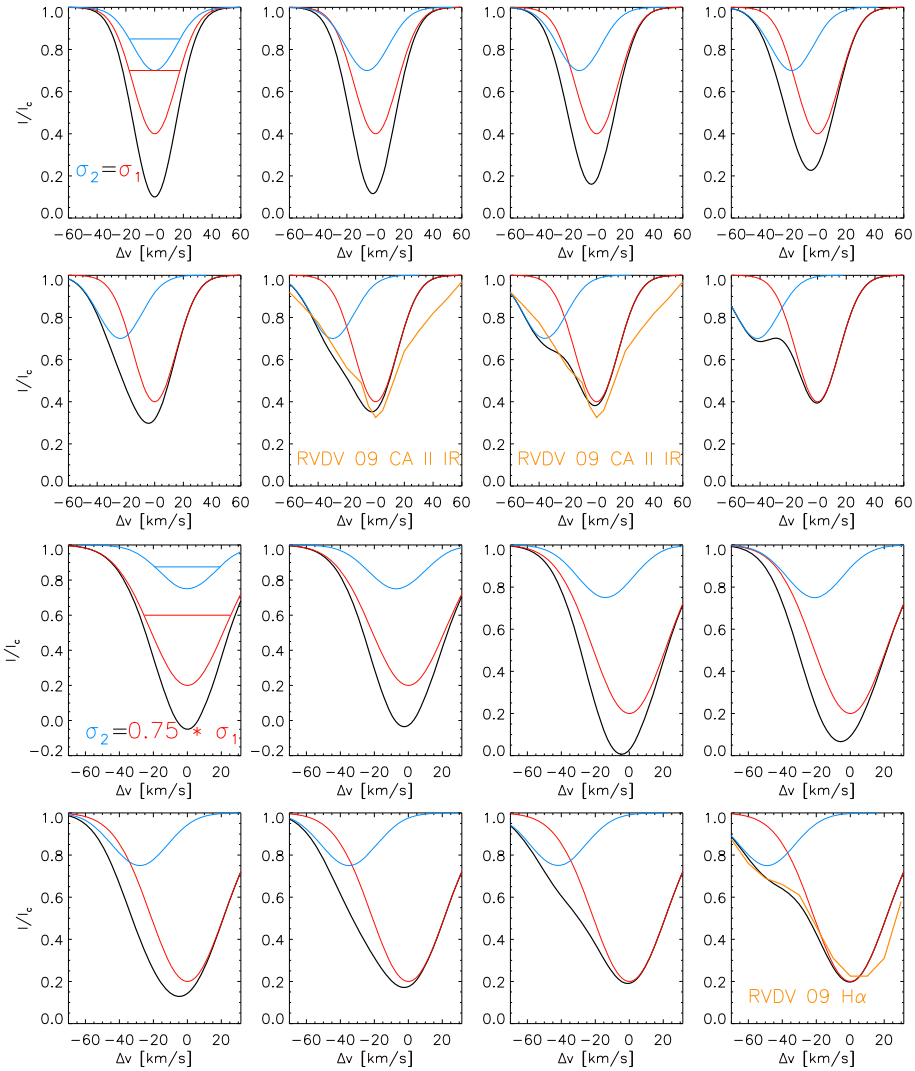

Figure 20 Reproduction of Ca II IR (top two rows) and Hα (bottom two rows) profiles observed in RBEs on-disk. Two Gaussians are overlayed in each panel. The red line corresponds to a non-shifted dominant component with a width σ_1, the blue line to a Doppler-shifted component with a width σ_2. The Doppler shift increases from left to right in each row. The orange line corresponds to the RBE profiles of Ca II IR and Hα in Figure 11 of Rouppe van der Voort *et al.* (2009), indicated as RVDV 09 in the corresponding panels. In the case of Ca II IR, the observed profile can be reproduced to first order with Gaussians of the same width, while for Hα a very good reproduction is achieved even if the width of the Doppler-shifted component is only 75 % of that of the component at rest.

the counterpart of spicules on the disk, show an increase in line width at their tips? For this, we have to take three points into account. First, the authors found a positive correlation between blueshift and line width (*e.g.*, their Figure 11); second, we have to consider their equation to determine the line width; and finally, we have to consider the shape of the profiles they found in RBEs (*e.g.*, their Figures 5, 9, and 11). Their RBE profiles show

clear indications of two different components: a dominating component with a small, or no, Doppler shift and a strongly blueshifted satellite of lower line depth (see also Peter, 2001; Tian *et al.*, 2011). The equation they used to determine the line width does not take the existence of these two components fully into account and corresponds more to a measure of line asymmetry than line width. Considering the line shape of the RBE profiles, the positive correlation between the velocity and the width directly follows: the larger the Doppler shift of the blueshifted component, the larger the line asymmetry. Figure 20 shows that asymmetric RBE profiles, as given in Rouppe van der Voort *et al.* (2009), can be generated without any increase in the line width in the Doppler-shifted component (compare also with the He I spectra in Figures 12, 18, and 19 of this article that do consist of two components). In the case of their RBE Hα profile, we can achieve a very good reproduction of the observed profile even if the width of the Doppler-shifted component is 25 % smaller than that of the non-shifted component. We therefore conclude that if such asymmetric profiles are typical for RBEs, they need not indicate an increased line width in the Doppler-shifted component, and hence also do not provide direct evidence for heating in RBEs.

6.3. Spicule Disappearance

The rather sharp boundary in height up to which spicules reach, the change of the line shape of the spectra with height, and the disappearance *in situ* can be explained by different effects. On the one hand, the emission in the respective line cores can disappear because there is not enough material left to generate a sufficient opacity, and hence the amplitude of the emission smoothly decreases to zero (*cf.* Figure 19). Because the density stratification in the quiet solar atmosphere can be assumed to be spatially rather homogeneous on large spatial or temporal scales, this would explain the sharp and well-defined upper limit in height above which almost no spicules can be seen. A second possibility is that the material becomes heated strongly and rapidly such that the necessary absorbers (or emitters) are lacking because the elements that cause the spectral lines are ionized to higher ionization states. This scenario has been invoked to explain spicules that fade away *in situ* (De Pontieu *et al.*, 2007b; Sterling, Moore, and DeForest, 2010) and implies that spicular material could act as an energy reservoir for the corona (De Pontieu *et al.*, 2009, 2011). The fact that counterparts to spicules are not always found in coronal lines (*e.g.* Madjarska, Vanninathan, and Doyle, 2011) might be mere chance (but see also Klimchuk, 2012). Finally, a third option would be that spicules consist of material that is shot up into the chromosphere to some height and that is hotter than the mass in the surroundings. The excess energy would then be lost by radiative cooling in the presumably optically thin environment, while the mass would generally follow a parabolic path of ascent and descent. On its path, the mass perturbation would temporally increase the density, hence the opacity and the emitted radiation would increase. This would cause the traveling mass to be visible in the same way as prominences or coronal rain (Antolin, Vissers, and Rouppe van der Voort, 2012; Oliver *et al.*, 2016) are detectable above the solar limb. It would lead to a sequential appearance and disappearance of spicules in low-forming (Ca II) and high-forming lines (Mg II, transition region), as described in Skogsrud *et al.* (2015) in terms of a passage of the material without requiring heating.

Can our multi-line spectra be used to distinguish between these possibilities? There is one argument in favor of a reduced density as the reason for the disappearance of spicules above a height of 6 Mm, instead of a rapid and strong heating to transition-region or coronal temperatures. The emission in both the Ca II IR line at 854.2 nm and the Hε line disappears in a way completely analogous to the disappearance in Ca II H, Hα, or He I at 1083 nm by

smoothly decreasing to zero with height. The former lines, however, disappear already at heights below 4 Mm (*cf.* Figure 18). It is therefore highly unlikely that a rapid and strong heating at a height of 4 Mm would only affect these two lines without any effect on the other lines from the same chemical elements, or without changing the line width of He I at 1083 nm at this height. We thus suggest that the sharp upper boundary for the appearance of spicules, if defined as elongated, thin structures, is only the consequence of the lack of emitters caused by the decreased density and does not indicate a heating to transition-region temperatures.

7. Conclusions

In an analysis of multiwavelength observations (Ca II H at 396.85 nm, Hε, Hα, Ca II IR at 854.2 nm, and He I at 1083 nm) of solar spicules at the limb, we found that spicules corresponding to the recently introduced type I or type II classes extend only up to a height of about 5 to 6 Mm. Structures above this height are mainly seen in Hα alone and differ from regular spicules by a significantly larger lateral width of up to a few Mm. All of the spectral lines show a decrease in the line width with height both in individual spicules, across the FOV, and in average profiles. A slight reversal of the trend at the uppermost tips occurs in spectra with very low intensities and was found to be spurious, being caused by the limitations of the data and their analysis. When we derived the kinetic temperature and non-thermal velocities, we found a decrease in both quantities with increasing limb distance. We therefore found no indications that the spicules in our data are gradually or rapidly heated to transition-region or coronal temperatures or that they extend to coronal heights.

Acknowledgements The VTT is operated by the Kiepenheuer-Institut für Sonnenphysik (KIS; Freiburg, Germany) at the Spanish Observatorio del Teide of the Instituto de Astrofísica de Canarias (IAC; La Laguna, Tenerife, Spain). POLIS was a joint development of the High Altitude Observatory (HAO; Boulder, USA) and the KIS. *Hinode* is a Japanese mission developed and launched by ISAS/JAXA, with NAOJ as domestic partner and NASA and STFC (UK) as international partners. It is operated by these agencies in cooperation with ESA and NSC (Norway). SOHO is a project of international cooperation between ESA and NASA. HMI data are courtesy of NASA/SDO and the HMI science team. R. Rezaei acknowledges financial support by the Deutsche Forschungsgemeinschaft under grant RE 3282/1-1. D. Fabbian acknowledges financial support by the Spanish Ministries of Research and Innovation and of Economy through projects AYA2011-24808 and CSD2007-00050.

Disclosure of Potential Conflicts of Interest The authors declare that they have no conflicts of interest.

Appendix A: 2D Spectroscopy in Hα

Figures 21 – 24 show the Hα line-core images recorded with TESOS during observations 2 and 3 in setup 1. Only the unsharp-masked images are shown. Both series are dominated by the appearance of large-scale structures of a few Mm lateral width at heights above 6 Mm (*e.g.*, inside the white rectangle in Figure 21). The first example (Figures 21 and 22) shows a complex evolution, where some material seems to be falling down toward the limb (white arrows in Figure 22), while at the same time several brightenings (red arrows in Figure 22) start to protrude next to the location where the falling mass reaches it lowest height. These two features, the falling mass and the extending brightenings, seem to merge together after-

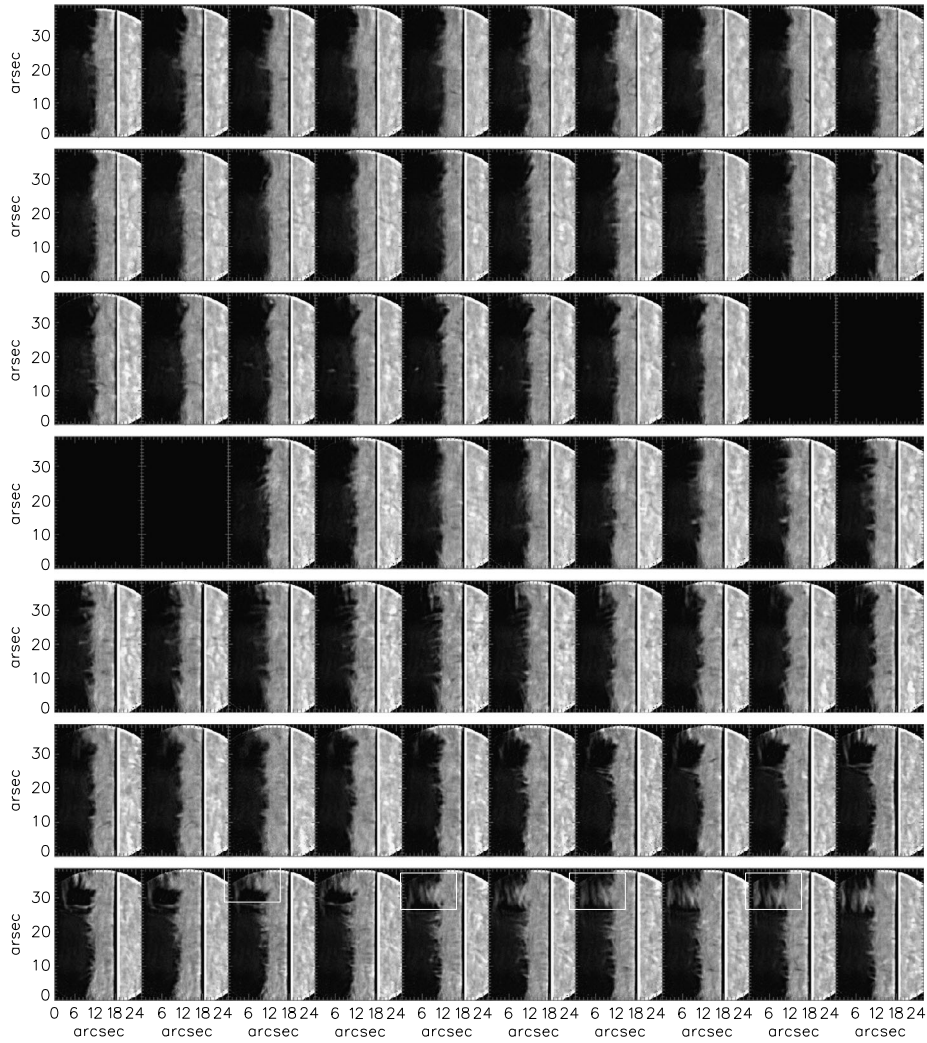

Figure 21 First half of the time series of Hα line-core images corresponding to observation 2 in Table 2. Only the image with unsharp masking is displayed. Time increases from left to right and top to bottom. The cadence between subsequent images is about 20 s. The white rectangle in the bottom row outlines a large-scale structure that extends beyond 6 Mm above the limb.

ward and eject a blob of material toward the corona (blue arrows in Figure 22). The ejected material rises upward until it leaves the FOV of the instrument. In the second example (Figures 23 and 24), a large-scale triangular structure with a large diameter above and a small diameter near the limb forms from a tree-like structure with two branches (white rectangles in Figure 23). The scenery is relatively quiet all throughout the FOV before, whereas with the appearance of the large-scale structure, several individual features appear above a height of 6 Mm that affect almost the full FOV of more than 20 Mm lateral extent at the same time. The large-scale structure is then unfortunately moved beyond the FOV by the sequential scanning of the solar image by the spectrograph instruments, so that the return

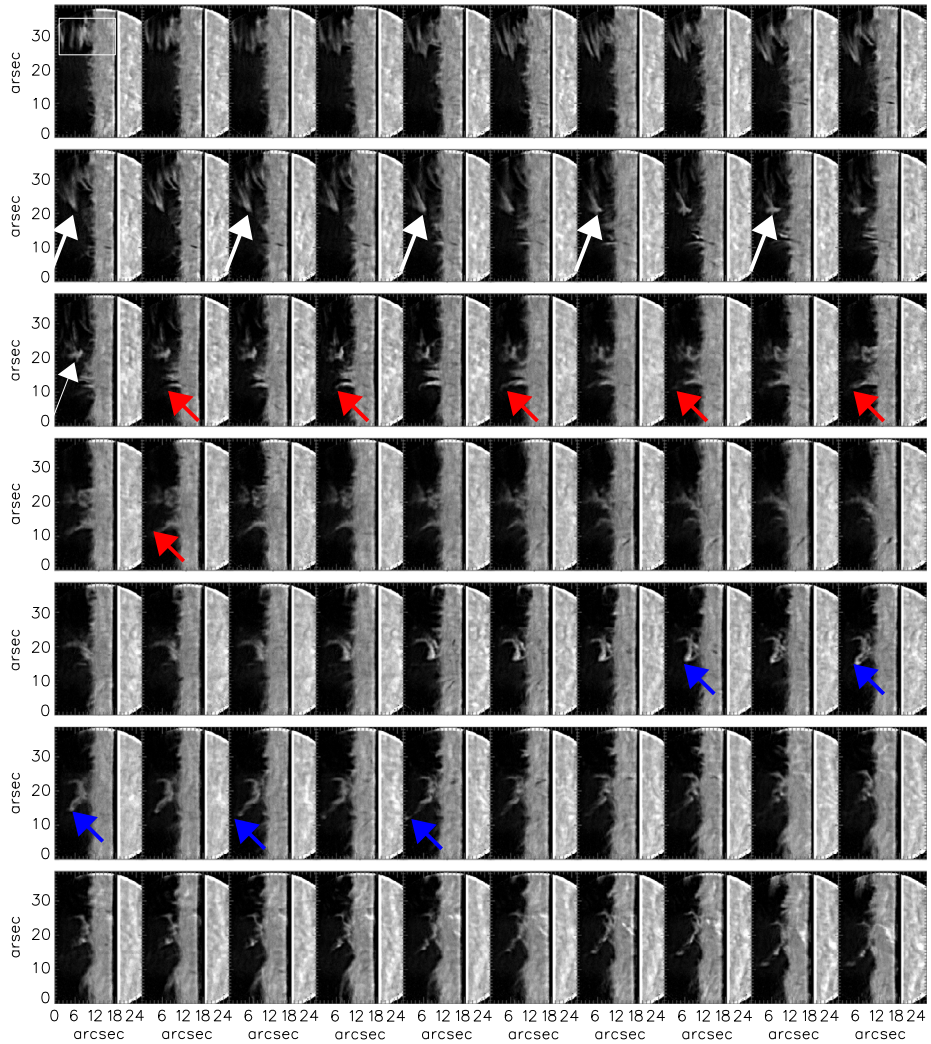

Figure 22 Second half of the time series of Hα line-core images corresponding to observation 2 in Table 2. Only the image with unsharp masking is displayed. Time increases from left to right and top to bottom. The cadence between subsequent images is about 20 s. The colored arrows indicate descending and rising features described in the text.

to a relatively quiet scene at the end might also be caused by this and not by a subsiding activity. The last images also show the degradation of the seeing during the observations.

Appendix B: Limitations of Gaussian Fits and Significance of the Results

B.1 Single- *vs.* Double-Gaussian Fit

The generally low light level beyond the limb, the decrease in the emission, and the residuals of the stray-light correction hamper any reliable analysis. For all observations and all

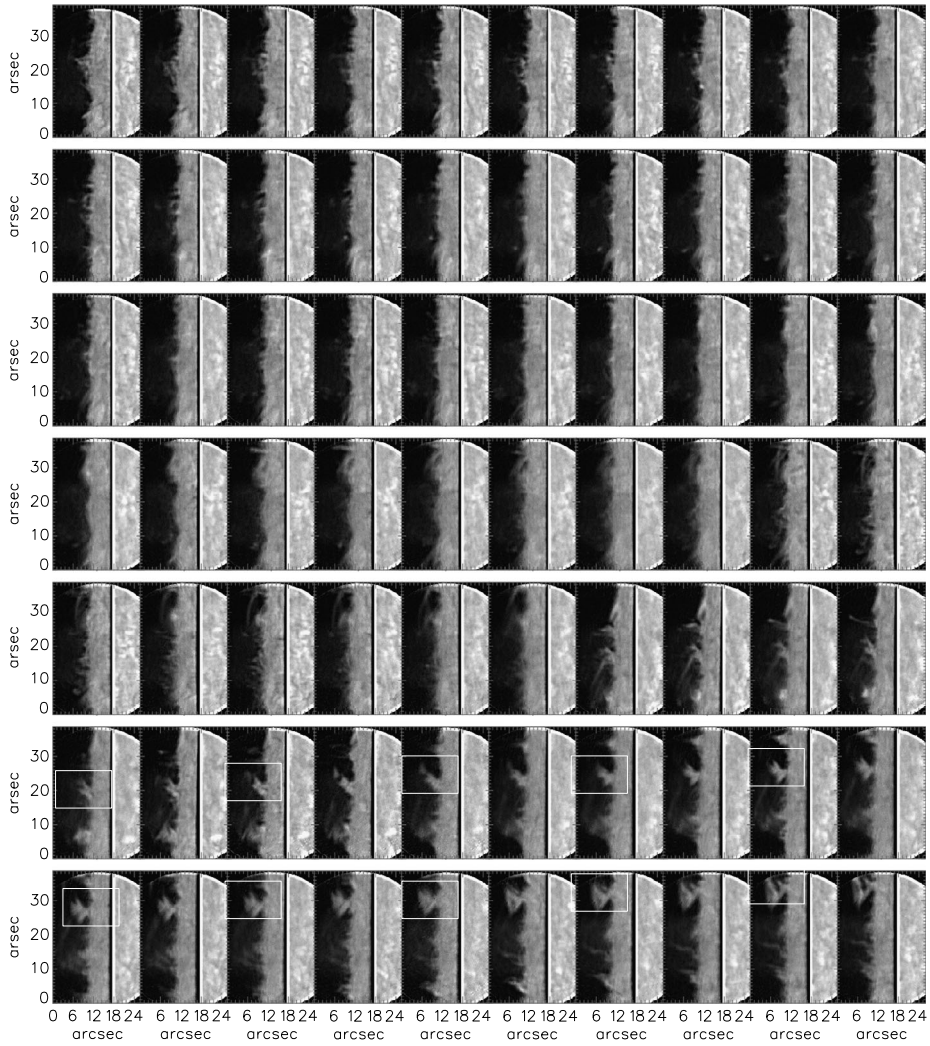

Figure 23 First part of the time series of Hα line-core images corresponding to observation 3 in Table 2. Only the image with unsharp masking is displayed. Time increases from left to right and top to bottom. The cadence between subsequent images is about 20 s. The white rectangle outlines a large-scale structure that extends beyond 6 Mm above the limb.

spectral lines, a single-Gaussian fit to all off-limb spectra was performed. All spectra with an amplitude of the Gaussian below a manually set threshold were rejected to remove profiles that contained only noise. To ensure that all significant profiles were kept, this threshold was set slightly lower than what would in principle be normal. For instance, for the He I at 1083 nm spectra of observation 1 the threshold level was chosen as 0.4 % of I_c, leading to the uniform black area in FWHM in Figure 14, third column, bottom panel. With this initial threshold, regions with a strongly increased FWHM in the results of the single-Gaussian fit remained significant (Figure 25). In the following, we investigate the corresponding profiles in more detail to show that the FWHM values derived from these profiles are spurious.

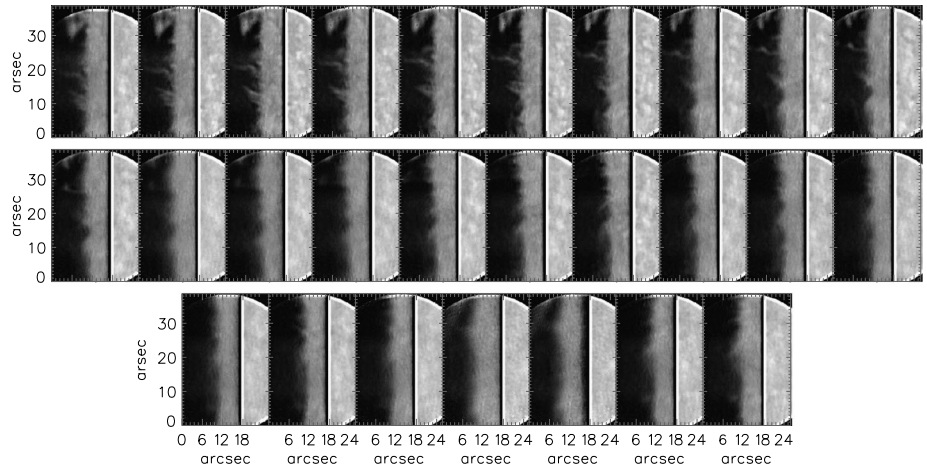

Figure 24 Second part of the time series of Hα line-core images corresponding to observation 3 in Table 2. Only the image with unsharp masking is displayed. Time increases from left to right and top to bottom. The cadence between subsequent images is about 20 s.

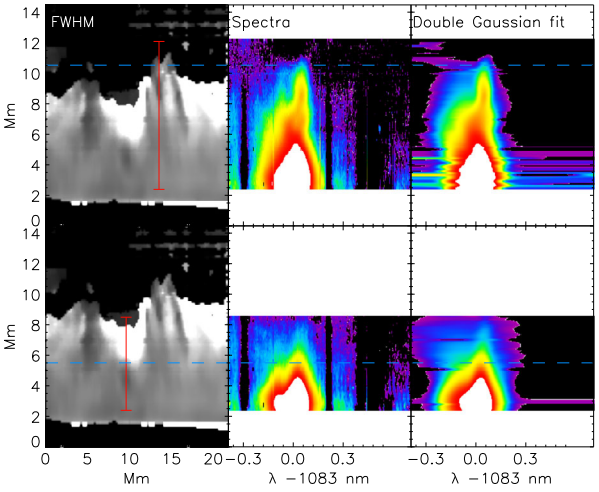

Figure 25 Quality of double-Gaussian fits. Left: FWHM from single-Gaussian fit. The red vertical bars mark the spatial location of the spectra shown in the other columns. The horizontal blue dashed lines denote the maximum extent to which the fits are deemed significant and reliable. Right two columns: spectra and double-Gaussian fits along the red bars in the left column. The values are displayed on a logarithmic scale, clipped, and in false color to highlight the shape at the lowest intensities.

Figure 25 shows the FWHM of He I at 1083 nm obtained from the single-Gaussian fit for observation 1. We selected two vertical cuts in the spectra across a region with strongly increased FWHM at low emission (bottom row) and across a spicule with high emission (top row). The spectra along these cuts (right panels of Figure 25) show that the emission pattern monotonically reduces both in amplitude and line width with increasing limb distance. In addition to the single-Gaussian fit, we ran a double-Gaussian fit over these profiles as well. Figure 26 shows every second individual profile along the cut of the bottom row of Figure 25 and the corresponding Gaussian fits. It is obvious that the single-Gaussian fit does not sample the main emission peak and becomes far too broad at about pixel 75 (towards smaller numbers). The double-Gaussian fit performs significantly better, but the true emission amplitude for profiles below about profile 69 is difficult to assess because it is comparable to the residual amplitude of, for example, the photospheric lines.

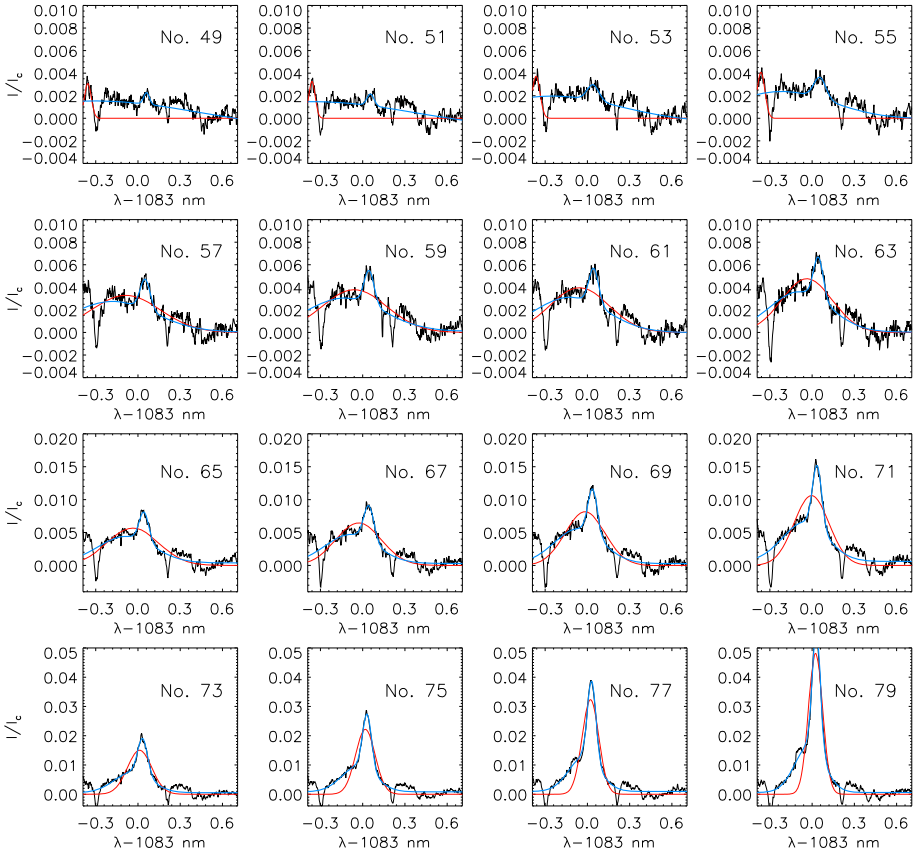

Figure 26 Gaussian fits to individual spectra. The observed spectra along the red bar in the lower row of Figure 25 are shown with black lines. Red and blue lines show the results of the single- and double-Gaussian fits. The two components of the double-Gaussian fit are shown separately in Figure 27. The single-Gaussian fit works up to about pixel 73. Decreasing numbers indicate increasing limb distance.

The individual components of the double-Gaussian fit are shown in Figure 27. One component (green lines) samples the emission peak, while the other captures some broad offset from zero that does not correspond to the blue component of the He emission pattern. For the case of the red emission component, the line width varies around 80 pm with no clear trend (profiles 57 – 73), with a slight increase relative to profiles 75 – 79. The variation comes, however, with the caveat that because of the limitations of the data, it is not obvious which part of the emission is genuine and which is spurious.

Figure 28 shows the FWHM for both the single- and double-Gaussian fits applied to the spectra selected in Figure 25. The substantial increase in line width in the single-Gaussian fit can be seen to be fully spurious for the first cut. It is represented by the second, broad component of the double-Gaussian fit that fits the continuum offset. Otherwise the FWHM for the main emission component in the double-Gaussian fit stays roughly constant with a slight decrease in the case of the cut along the spicule.

Given the limitations of the data and the analysis as discussed above, we therefore find the strong increase in FWHM in the He I at 1083 nm spectra, and likewise in the other lines because the line shapes are similar at some height, to be spurious. For low-amplitude profiles,

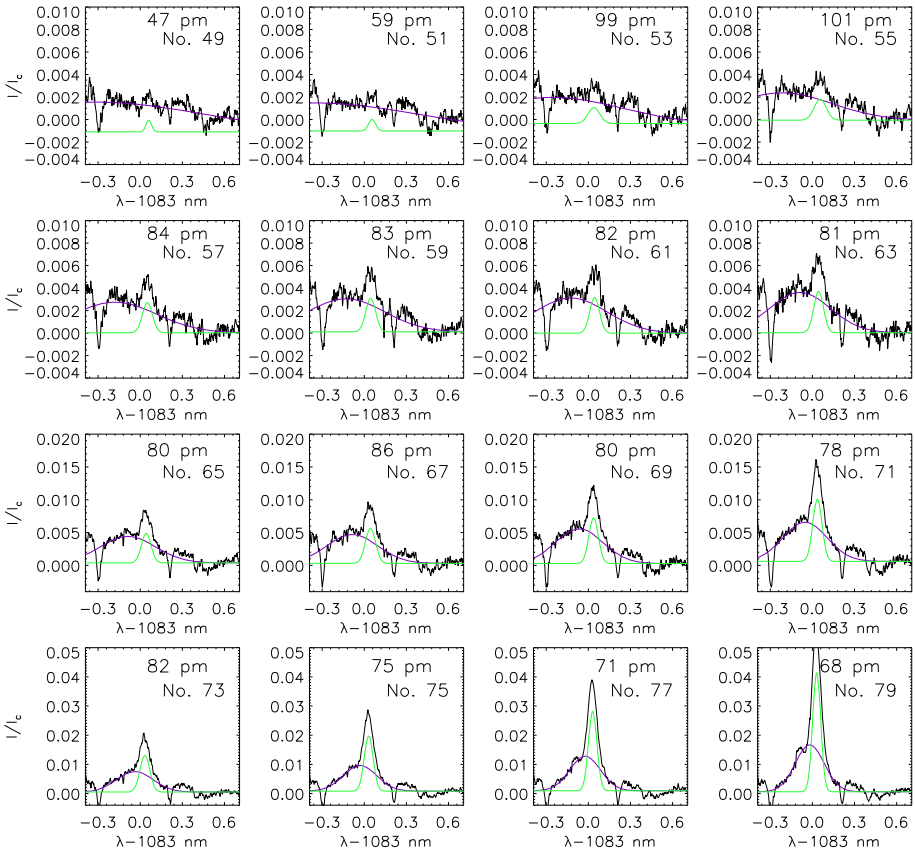

Figure 27 Double-Gaussian fit to individual spectra. The observed spectra along the red bar in the lower row of Figure 25 are shown with black lines. Green and purple lines show the two components of the double-Gaussian fit. The values at the upper right corner in each panel give the FWHM of the main (green) component.

the Gaussian fits might be more misleading than a direct look at the corresponding profiles (Figures 4, 7, 8, 11, 12, 18, 19, and 25). The latter reveals a decrease in line width up to the point where residuals of photospheric blends are as strong as the chromospheric emission.

B.2 Influence of the Blue Component at 1082.91 nm

The He line at 1083 nm consists of two main components at nearby wavelengths at 1082.91 nm and 1083.03 nm (see, for instance, Sánchez-Andrade Nuño *et al.*, 2007). The ratio of the two components $I_{\rm blue}/I_{\rm red}$ is about 8 in the optically thin case, but can decrease to 3 at a height of about 2 Mm above the limb before approaching the optically thin case again at larger limb distances (Sánchez-Andrade Nuño *et al.*, 2007, their Figure 4). Figure 29 shows that the influence of the weaker blue component on the fit of the red component with a single Gaussian is minor, in contrast to the residuals from the stray-light correction discussed in the previous section for profiles with a low light level far from the limb. The line width of the stronger red component of the spectra is well recovered by the single-Gaussian fit for all profiles closer to the limb than $d < 6$ Mm (profiles 80 or more in Figure 29; emission

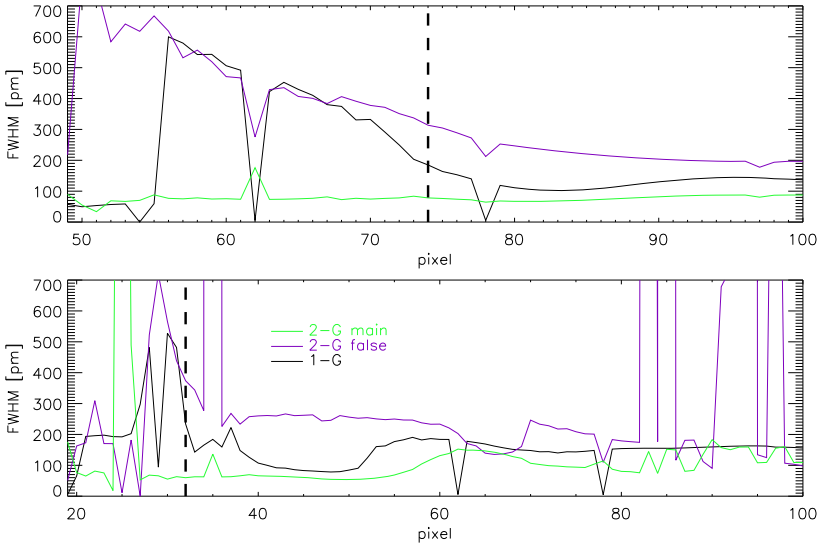

Figure 28 Comparison of FWHM from single- and double-Gaussian fits. Top and bottom panel: FWHM of the spectra shown in the bottom and top row of Figure 25. Black lines: single-Gaussian (1-G) fit. Green line: main component of double-Gaussian (2-G) fit. Purple line: spurious component of double-Gaussian (2-G false) fit (see Figure 27). The vertical black dashed lines denote the maximum extent to which the fits are deemed significant and correspond to the blue lines in Figure 25.

amplitude 5 % or higher). The weaker blue component has little effect on the fit because of its much smaller amplitude. The different amplitude of the components justifies the use of only a single Gaussian for the automated analysis of the spectra across the FOV even if the He line consists of multiple components.

Appendix C: Observations 2 – 4

The top panel of Figure 30 shows the results of the Gaussian fit to the Ca II H and He I spectra of observation 2. This observation was selected because its long integration time of 60 s allows us to trace features of very low intensities as well. The corresponding Hα line-core images in Figures 21 and 22 show that during this scan a large-scale (width and height of $\approx$4 Mm $\times$ 13 Mm) structure with a complex temporal evolution moved across the FOV. The slit-spectrograph data in this case failed to capture the temporal evolution and only record the sheer height extent of the structure up to 13 Mm above the limb. Thanks to the long integration time, even the spectra far away from the limb can still be reliably analyzed. The plot of FWHM in the bottom panel of Figure 30 confirms the visual impression of the top panel: the FWHM in Ca II H monotonically decreases up to the top of the feature. Above about $y \approx 8$ Mm, the feature presumably is the only one existing at that height, so that the monotonic decline of the FWHM does not indicate a possible decrease in the overlap of different features along the LOS. For He I at 1083 nm, the FWHM shows a rise at the top, but in the corresponding maps of He I line-core intensity or the amplitude of the Gaussian, the intensity above 11 Mm is virtually zero.

The top panel of Figure 31 shows the results of the Gaussian fit to the Ca II H and He I spectra of observation 3, while the corresponding Hα line-core images are shown in Fig-

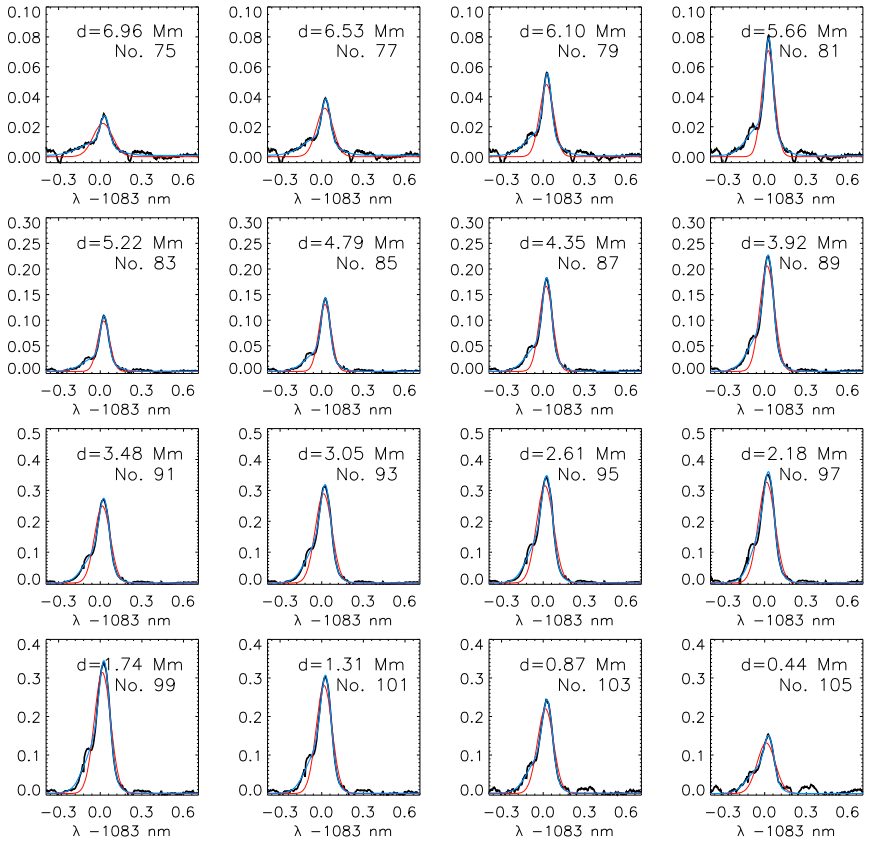

Figure 29 Gaussian fits to individual He I 1083 nm spectra from the limb to a height of about 7 Mm. The observed spectra are shown with black lines. Red and blue lines show the results of the single- and double-Gaussian fits. The limb distance d is given at the top in each panel.

ures 23 and 24. Similar to observation 3, the Hα line-core images exhibit mainly complex-shaped structures without much resemblance to spicules at heights larger than 5 Mm above the limb. None of these features are captured in the Ca II H spectra, which drop to zero intensity everywhere throughout the FOV above that height (top row of Figure 31), whereas the He I spectra still sampled them up to about 10 Mm above the limb. The FWHM of Ca II H shows a rather uniform decrease with height above the limb. The FWHM of the He I line at 1083 nm shows again a mainly lateral structuring with little vertical variation. At the location used for a vertical cut in the He I spectra, the FWHM decreases monotonically up to about 10 Mm above the limb (bottom panel of Figure 31).

The last example of the 2010 data (observation 4, Figure 32) was taken with the slit oriented parallel to the limb that is located just at the bottom border of the FOV. We were unable to apply any correction for stray light to these data because of the limited extent of the FOV that neither contains a sufficiently large on-disk region nor a suitable off-limb area for calculating an average profile to be used in the stray-light correction. A few features can be called distinguishable (at $x \approx 20$, 28 and 33 Mm) in the line-core image or the intensity of the H_{2V} emission peak. The temporal evolution of their FWHM shows no indication of a

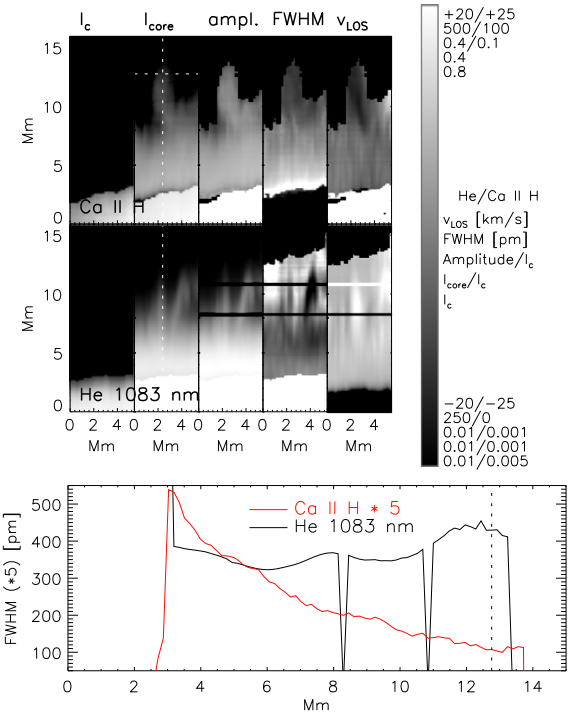

Figure 30 Top panel: results of the Gaussian fit in Ca II H and He I at 1083 nm for observation 2 with a 60 s integration time. Bottom panel: FWHM in Ca II H and He I at 1083 nm along the vertical dotted line in the top panel. The horizontal dotted line in the top panel and the vertical dotted line the bottom panel denote the broadest range with spectra above the noise level. The gray bar at the right gives the lowest (at the bottom) and highest (at the top) values for (left to right) He I at 1083 nm and Ca II H for (bottom to top) the continuum intensity, line-core intensity, emission amplitude, FWHM, and LOS velocity. The same range was used for both lines wherever only one value is provided.

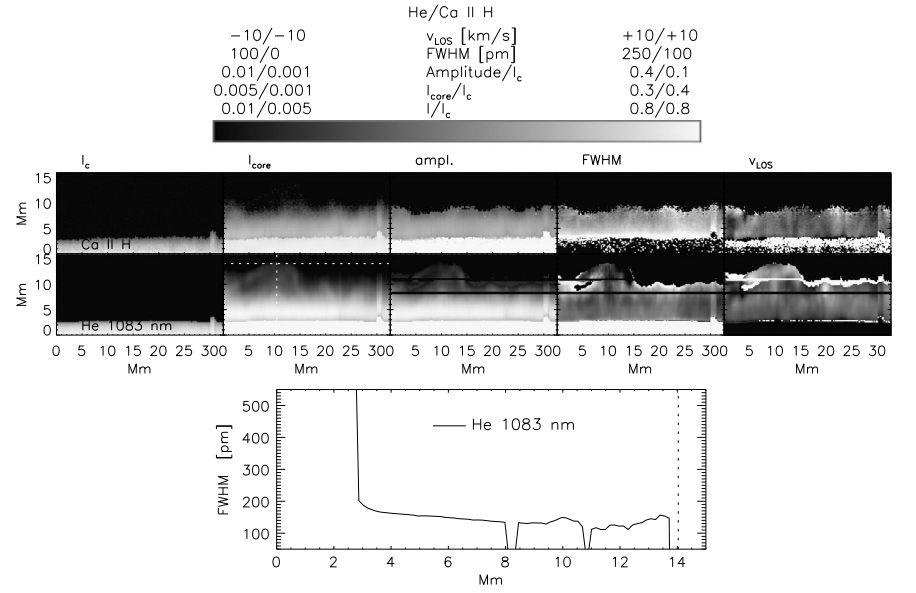

Figure 31 Top: results of the Gaussian fit in Ca II H and He I at 1083 nm for observation 3. Bottom: FWHM in He I at 1083 nm along the vertical dotted line in the top panel. The horizontal dotted line in the top panel and the vertical dotted line the bottom panel denote the broadest range with spectra above the noise level. The gray bar at the top gives the lowest (at the left-hand side) and highest (at the right-hand side) values for (left and right) He I at 1083 nm and Ca II H for (bottom to top) the continuum intensity, line-core intensity, emission amplitude, FWHM, and LOS velocity.

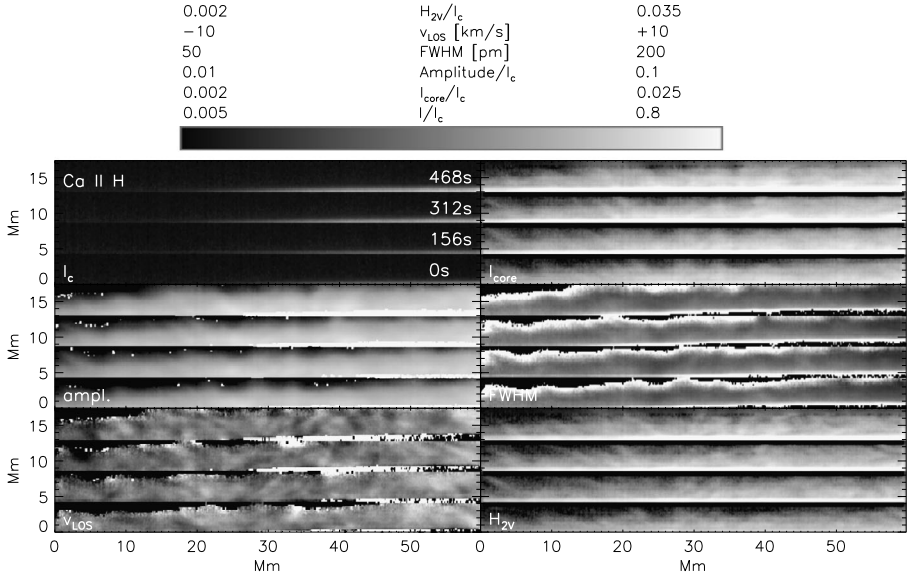

Figure 32 Results of the Gaussian fit in Ca II H for observation 4. Left column, top to bottom: continuum intensity, amplitude, and LOS velocity. Right column, top to bottom: line-core intensity, FWHM, and intensity of the H_{2V} emission peak. Here x corresponds to the direction along the slit and y to the scanning direction, in contrast to the previous figures. The four panels in y for each quantity correspond to four repetitions of the scan taken with a cadence of 156 s. The gray bar at the top gives the lowest (at the left-hand side) and highest (at the right-hand side) values for Ca II H for (bottom to top) the continuum intensity, line-core intensity, emission amplitude, FWHM, LOS velocity, and the H_{2V} emission amplitude.

significant change with time or height above the limb within the limitations of cadence and spatial resolution.

References

Alissandrakis, C.E.: 1973, A spectroscopic study of solar spicules in Hα, Hβ and K. *Solar Phys.* **32**, 345. DOI. ADS.

Anan, T., Kitai, R., Kawate, T., Matsumoto, T., Ichimoto, K., Shibata, K., Hillier, A., Otsuji, K., Watanabe, H., Ueno, S., Nagata, S., Ishii, T.T., Komori, H., Nishida, K., Nakamura, T., Isobe, H., Hagino, M.: 2010, Spicule dynamics over a plage region. *Publ. Astron. Soc. Japan* **62**, 871. DOI. ADS.

Antolin, P., Vissers, G., Rouppe van der Voort, L.: 2012, On-disk coronal rain. *Solar Phys.* **280**, 457. DOI. ADS.

Athay, R.G.: 2000, Are spicules related to coronal heating? *Solar Phys.* **197**, 31. DOI. ADS.

Athay, R.G., Holzer, T.E.: 1982, The role of spicules in heating the solar atmosphere. *Astrophys. J.* **255**, 743. DOI. ADS.

Avery, L.W.: 1970, The formation of the Ca II K line in a spinning spicule. *Solar Phys.* **13**, 301. DOI. ADS.

Beck, C.A.R., Rezaei, R.: 2011, Spectroscopy at the solar limb. I. Average off-limb profiles and Doppler shifts of Ca II H. *Astron. Astrophys.* **531**, A173. DOI. ADS.

Beck, C., Rezaei, R.: 2012, Chromospheric multi-wavelength observations near the solar limb: Techniques and prospects. In: Rimmele, T.R., Tritschler, A., Wöger, F., Collados Vera, M., Socas-Navarro, H., Schlichenmaier, R., Carlsson, M., Berger, T., Cadavid, A., Gilbert, P.R., Goode, P.R., Knölker, M. (eds.) *Magnetic Fields from the Photosphere to the Corona*, *Astron. Soc. Pacific Conf. Ser.* **463**, 257. ADS.

Beck, C., Rezaei, R., Fabbian, D.: 2011, Stray-light contamination and spatial deconvolution of slit-spectrograph observations. *Astron. Astrophys.* **535**, A129. DOI. ADS.

Beck, C., Rezaei, R., Puschmann, K.G.: 2013, Can spicules be detected at disc centre in broad-band Ca II H filter imaging data? *Astron. Astrophys.* **556**, A127. DOI. ADS.

Beck, C., Schmidt, W., Kentischer, T., Elmore, D.: 2005, Polarimetric littrow spectrograph – Instrument calibration and first measurements. *Astron. Astrophys.* **437**, 1159. DOI. ADS.
Beck, C., Bellot Rubio, L.R., Schlichenmaier, R., Sütterlin, P.: 2007, Magnetic properties of G-band bright points in a sunspot moat. *Astron. Astrophys.* **472**, 607. DOI. ADS.
Beck, C., Schmidt, W., Rezaei, R., Rammacher, W.: 2008, The signature of chromospheric heating in Ca II H spectra. *Astron. Astrophys.* **479**, 213. DOI. ADS.
Beck, C., Fabbian, D., Moreno-Insertis, F., Puschmann, K.G., Rezaei, R.: 2013, Thermodynamic fluctuations in solar photospheric three-dimensional convection simulations and observations. *Astron. Astrophys.* **557**, A109. DOI. ADS.
Beckers, J.M.: 1968, Solar spicules (Invited Review Paper). *Solar Phys.* **3**, 367. DOI. ADS.
Beckers, J.M.: 1972, Solar spicules. *Annu. Rev. Astron. Astrophys.* **10**, 73. DOI. ADS.
Bendlin, C., Wiehr, E., Stellmacher, G.: 1988, Spectroscopic analysis of prominence emissions. *Astron. Astrophys.* **197**, 274. ADS.
Berger, T.E., Shine, R.A., Slater, G.L., Tarbell, T.D., Title, A.M., Okamoto, T.J., Ichimoto, K., Katsukawa, Y., Suematsu, Y., Tsuneta, S., Lites, B.W., Shimizu, T.: 2008, Hinode SOT observations of solar quiescent prominence dynamics. *Astrophys. J. Lett.* **676**, L89. DOI. ADS.
Bohlin, J.D., Vogel, S.N., Purcell, J.D., Sheeley, N.R. Jr., Tousey, R., Vanhoosier, M.E.: 1975, A newly observed solar feature – Macrospicules in He II 304 A. *Astrophys. J. Lett.* **197**, L133. DOI. ADS.
Cabrera Solana, D., Bellot Rubio, L.R., Beck, C., Del Toro Iniesta, J.C.: 2007, Temporal evolution of the Evershed flow in sunspots. I. Observational characterization of Evershed clouds. *Astron. Astrophys.* **475**, 1067. DOI. ADS.
Casini, R., López Ariste, A., Tomczyk, S., Lites, B.W.: 2003, Magnetic maps of prominences from full Stokes analysis of the He I D3 line. *Astrophys. J. Lett.* **598**, L67. DOI. ADS.
Cavallini, F.: 2006, IBIS: A new post-focus instrument for solar imaging spectroscopy. *Solar Phys.* **236**, 415. DOI. ADS.
Centeno, R., Trujillo Bueno, J., Asensio Ramos, A.: 2010, On the magnetic field of off-limb spicules. *Astrophys. J.* **708**, 1579. DOI. ADS.
Collados, M., Lagg, A., Díaz García, J.J., Hernández Suárez, E., López López, R., Páez Mañá, E., Solanki, S.K.: 2007, Tenerife infrared polarimeter II. In: Heinzel, P., Dorotovič, I., Rutten, R.J. (eds.) *The Physics of Chromospheric Plasmas*, *Astron. Soc. Pacific Conf. Ser.* **368**, 611. ADS.
Collados, M., Bettonvil, F., Cavaller, L., Ermolli, I., Gelly, B., Grivel-Gelly, C., Pérez, A., Socas-Navarro, H., Soltau, D., Volkmer, R.: 2010, European solar telescope: Project status. In: Stepp, L.M., Gilmozzi, R., Hall, H.J. (eds.) *Ground-Based and Airborne Telescopes III*, *SPIE Conf. Ser.* **7733**, 77330H. DOI. ADS.
De Pontieu, B., Haerendel, G.: 1998, Weakly damped Alfven waves as drivers for spicules. *Astron. Astrophys.* **338**, 729. ADS.
De Pontieu, B., Erdélyi, R., James, S.P.: 2004, Solar chromospheric spicules from the leakage of photospheric oscillations and flows. *Nature* **430**, 536. ADS. DOI.
De Pontieu, B., Hansteen, V.H., Rouppe van der Voort, L., van Noort, M., Carlsson, M.: 2007a, High-resolution observations and numerical simulations of chromospheric fibrils and mottles. In: Heinzel, P., Dorotovič, I., Rutten, R.J. (eds.) *The Physics of Chromospheric Plasmas*, *Astron. Soc. Pacific Conf. Ser.* **368**. ADS.
De Pontieu, B., McIntosh, S., Hansteen, V.H., Carlsson, M., Schrijver, C.J., Tarbell, T.D., Title, A.M., Shine, R.A., Suematsu, Y., Tsuneta, S., Katsukawa, Y., Ichimoto, K., Shimizu, T., Nagata, S.: 2007b, A tale of two spicules: The impact of spicules on the magnetic chromosphere. *Publ. Astron. Soc. Japan* **59**, S655. DOI. ADS.
De Pontieu, B., McIntosh, S.W., Hansteen, V.H., Schrijver, C.J.: 2009, Observing the roots of solar coronal heating in the chromosphere. *Astrophys. J. Lett.* **701**, L1. DOI. ADS.
De Pontieu, B., Carlsson, M., Rouppe van der Voort, L.H.M., Rutten, R.J., Hansteen, V.H., Watanabe, H.: 2012, Ubiquitous torsional motions in type II spicules. *Astrophys. J. Lett.* **752**, L12. DOI. ADS.
De Pontieu, B., McIntosh, S.W., Carlsson, M., Hansteen, V.H., Tarbell, T.D., Boerner, P., Martinez-Sykora, J., Schrijver, C.J., Title, A.M.: 2011, The origins of hot plasma in the solar corona. *Science* **331**. DOI. ADS.
Dunn, R.B.: 1964, An evacuated tower telescope. *Appl. Opt.* **3**, 1353. DOI. ADS.
Dunn, R.B., Smartt, R.N.: 1991, High resolution telescopes at the National Solar Observatory. *Adv. Space Res.* **11**, 139. DOI. ADS.
Engvold, O., Halvorsen, H.D.: 1973, New identifications of disk emission lines in the Ca II H and K line wings. *Solar Phys.* **28**, 23. DOI. ADS.
Felipe, T., Khomenko, E., Collados, M., Beck, C.: 2010, Multi-layer study of wave propagation in sunspots. *Astrophys. J.* **722**, 131. DOI. ADS.

Gandorfer, A.M., Steiner, H.P.P.P., Aebersold, F., Egger, U., Feller, A., Gisler, D., Hagenbuch, S., Stenflo, J.O.: 2004, Solar polarimetry in the near UV with the Zurich Imaging Polarimeter ZIMPOL II. *Astron. Astrophys.* **422**, 703. DOI. ADS.

Goodman, M.L.: 2012, Acceleration of type II spicules in the solar chromosphere. *Astrophys. J.* **757**, 188. DOI. ADS.

Grossmann-Doerth, U., Schmidt, W.: 1992, Chromospheric fine structure revisited. *Astron. Astrophys.* **264**, 236. ADS.

Guerreiro, N., Carlsson, M., Hansteen, V.: 2013, Numerical simulations of spicule acceleration. *Astrophys. J.* **766**, 128. DOI. ADS.

Hammer, R., Musielak, Z.E., Routh, S., Nesis, A.: 2008, Spicules: Energetics and the role of magnetic waves. In: Peter, H. (ed.) *12th European Solar Phys. Meeting* **12**, 3. ADS.

Hansteen, V.H., De Pontieu, B., Rouppe van der Voort, L., van Noort, M., Carlsson, M.: 2006, Dynamic fibrils are driven by magnetoacoustic shocks. *Astrophys. J. Lett.* **647**, L73. DOI. ADS.

He, J.-S., Tu, C.-Y., Marsch, E., Guo, L.-J., Yao, S., Tian, H.: 2009, Upward propagating high-frequency Alfvén waves as identified from dynamic wave-like spicules observed by SOT on Hinode. *Astron. Astrophys.* **497**, 525. DOI. ADS.

Heggland, L., De Pontieu, B., Hansteen, V.H.: 2009, Observational signatures of simulated reconnection events in the solar chromosphere and transition region. *Astrophys. J.* **702**, 1. DOI. ADS.

Henriques, V.M.J., Kuridze, D., Mathioudakis, M., Keenan, F.P.: 2016, Quiet-Sun Hα transients and corresponding small-scale transition region and coronal heating. *Astrophys. J.* **820**, 124. DOI. ADS.

Hollweg, J.V.: 1982, On the origin of solar spicules. *Astrophys. J.* **257**, 345. DOI. ADS.

Jess, D.B., Mathioudakis, M., Christian, D.J., Keenan, F.P., Ryans, R.S.I., Crockett, P.J.: 2010, ROSA: A high-cadence, synchronized multi-camera solar imaging system. *Solar Phys.* **261**, 363. DOI. ADS.

Jess, D.B., Pascoe, D.J., Christian, D.J., Mathioudakis, M., Keys, P.H., Keenan, F.P.: 2012, The origin of type I spicule oscillations. *Astrophys. J. Lett.* **744**, L5. DOI. ADS.

Judge, P.G., Carlsson, M.: 2010, On the solar chromosphere observed at the LIMB with hinode. *Astrophys. J.* **719**, 469. DOI. ADS.

Judge, P.G., de Pontieu, B., McIntosh, S.W., Olluri, K.: 2012, The connection of type II spicules to the corona. *Astrophys. J.* **746**, 158. DOI. ADS.

Kamio, S., Curdt, W., Teriaca, L., Inhester, B., Solanki, S.K.: 2010, Observations of a rotating macrospicule associated with an X-ray jet. *Astron. Astrophys.* **510**, L1. DOI. ADS.

Kentischer, T.J., Schmidt, W., Sigwarth, M., Uexkuell, M.V.: 1998, TESOS, a double Fabry–Pérot instrument for solar spectroscopy. *Astron. Astrophys.* **340**, 569. ADS.

Klimchuk, J.A.: 2012, The role of type II spicules in the upper solar atmosphere. *J. Geophys. Res.* **117**(A16), 12102. DOI. ADS.

Kosugi, T., Matsuzaki, K., Sakao, T., Shimizu, T., Sone, Y., Tachikawa, S., Hashimoto, T., Minesugi, K., Ohnishi, A., Yamada, T., Tsuneta, S., Hara, H., Ichimoto, K., Suematsu, Y., Shimojo, M., Watanabe, T., Shimada, S., Davis, J.M., Hill, L.D., Owens, J.K., Title, A.M., Culhane, J.L., Harra, L.K., Doschek, G.A., Golub, L.: 2007, The hinode (solar-B) mission: An overview. *Solar Phys.* **243**, 3. DOI. ADS.

Kudoh, T., Shibata, K.: 1999, Alfvén wave model of spicules and coronal heating. *Astrophys. J.* **514**, 493. DOI. ADS.

Kukhianidze, V., Zaqarashvili, T.V., Khutsishvili, E.: 2006, Observation of kink waves in solar spicules. *Astron. Astrophys.* **449**, L35. DOI. ADS.

Kulidzanishvili, V.I., Zhugzhda, I.D.: 1983, On the problem of spicular oscillations. *Solar Phys.* **88**, 35. DOI. ADS.

Kurucz, R.L., Furenlid, I., Brault, J., Testerman, L.: 1984, Solar flux atlas from 296 to 1300 nm. In: *Sunspot*, National Solar Obs., New Mexico, ADS.

Langangen, Ø., De Pontieu, B., Carlsson, M., Hansteen, V.H., Cauzzi, G., Reardon, K.: 2008, Search for high velocities in the disk counterpart of type II spicules. *Astrophys. J. Lett.* **679**, L167. DOI. ADS.

Lites, B.W.: 1974, The solar fen 2L 3969. 4 disk emission line. *Astron. Astrophys.* **33**, 363. ADS.

Löfdahl, M.G.: 2002, Multi-frame blind deconvolution with linear equality constraints. In: Bones, P.J., Fiddy, M.A., Millane, R.P. (eds.) *Image Reconstruction from Incomplete Data*, *SPIE Conf. Ser.* **4792**, 146. DOI. ADS.

Löfdahl, M.G., Scharmer, G.B.: 2012, Sources of straylight in the post-focus imaging instrumentation of the Swedish 1-m solar telescope. *Astron. Astrophys.* **537**, A80. DOI. ADS.

López Ariste, A., Casini, R.: 2005, Inference of the magnetic field in spicules from spectropolarimetry of He I D3. *Astron. Astrophys.* **436**, 325. DOI. ADS.

López Ariste, A., Rayrole, J., Semel, M.: 2000, First results from THEMIS spectropolarimetric mode. *Astron. Astrophys. Suppl.* **142**, 137. DOI. ADS.

Madjarska, M.S., Vanninathan, K., Doyle, J.G.: 2011, Can coronal hole spicules reach coronal temperatures? *Astron. Astrophys.* **532**, L1. DOI. ADS.

Makita, M.: 2003, Chromospheric structure derived from flash spectra of the total solar eclipse. *Publ. Natl. Astron. Obs. Jpn.* **7**, 1. ADS.

Martínez González, M.J., Asensio Ramos, A., Manso Sainz, R., Beck, C., Belluzzi, L.: 2012, Anomalous circular polarization profiles in the He I 1083.0 nm multiplet from solar spicules. *Astrophys. J.* **759**, 16. DOI. ADS.

Martinez Pillet, V.: 1992, Stray-light effects on the solar intensity distribution. *Solar Phys.* **140**, 207. DOI. ADS.

Mártinez Pillet, V., Collados, M., Sánchez Almeida, J., González, V., Cruz-Lopez, A., Manescau, A., Joven, E., Paez, E., Diaz, J., Feeney, O., Sánchez, V., Scharmer, G., Soltau, D.: 1999, LPSP & TIP: Full Stokes polarimeters for the Canary Islands observatories. In: Rimmele, T.R., Balasubramaniam, K.S., Radick, R.R. (eds.) *High Resolution Solar Physics: Theory, Observations, and Techniques*, *Astron. Soc. Pacific Conf. Ser.* **183**, 264. ADS.

Martínez-Sykora, J., Hansteen, V., Moreno-Insertis, F.: 2011, On the origin of the type II spicules: Dynamic three-dimensional MHD simulations. *Astrophys. J.* **736**, 9. DOI. ADS.

Martínez-Sykora, J., Hansteen, V., DePontieu, B., Carlsson, M.: 2009, Spicule-like structures observed in three-dimensional realistic magnetohydrodynamic simulations. *Astrophys. J.* **701**, 1569. DOI. ADS.

Matsuno, K., Hirayama, T.: 1988, The height distribution of the kinetic temperature and turbulent velocity of solar H-alpha spicules. *Solar Phys.* **117**, 21. DOI. ADS.

Mattig, W.: 1983, On the instrumental and atmospheric stray-light for solar observations. *Solar Phys.* **87**, 187. DOI. ADS.

McIntosh, S.W., De Pontieu, B.: 2009, Observing episodic coronal heating events rooted in chromospheric activity. *Astrophys. J. Lett.* **706**, L80. DOI. ADS.

Murawski, K., Srivastava, A.K., Zaqarashvili, T.V.: 2011, Numerical simulations of solar macrospicules. *Astron. Astrophys.* **535**, A58. DOI. ADS.

Neckel, H.: 1999, Announcement. *Solar Phys.* **184**, 421. DOI. ADS.

Nishikawa, T.: 1988, Spicule observations with high spatial resolution. *Publ. Astron. Soc. Japan* **40**, 613. ADS.

Oliver, R., Soler, R., Terradas, J., Zaqarashvili, T.V.: 2016, Dynamics of coronal rain and descending plasma blobs in solar prominences. II. Partially ionized case. *Astrophys. J.* **818**, 128. DOI. ADS.

Orozco Suárez, D., Asensio Ramos, A., Trujillo Bueno, J.: 2015, Height variation of the vector magnetic field in solar spicules. *Astrophys. J. Lett.* **803**, L18. DOI. ADS.

Paletou, F., López Ariste, A., Bommier, V., Semel, M.: 2001, Full-Stokes spectropolarimetry of solar prominences. *Astron. Astrophys.* **375**, L39. DOI. ADS.

Pasachoff, J.M.: 1970, Fine structure in Ca II on the solar disc. *Solar Phys.* **12**, 202. DOI. ADS.

Pasachoff, J.M., Jacobson, W.A., Sterling, A.C.: 2009, Limb spicules from the ground and from space. *Solar Phys.* **260**, 59. DOI. ADS.

Pasachoff, J.M., Noyes, R.W., Beckers, J.M.: 1968, Spectral observations of spicules at two heights in the solar chromosphere. *Solar Phys.* **5**, 131. DOI. ADS.

Pasachoff, J.M., Zirin, H.: 1971, On K-line central reversals. *Solar Phys.* **18**, 27. DOI. ADS.

Pereira, T.M.D., De Pontieu, B., Carlsson, M.: 2012, Quantifying spicules. *Astrophys. J.* **759**, 18. DOI. ADS.

Pereira, T.M.D., De Pontieu, B., Carlsson, M.: 2013, The effects of spatio-temporal resolution on deduced spicule properties. *Astrophys. J.* **764**, 69. DOI. ADS.

Pereira, T.M.D., Rouppe van der Voort, L., Carlsson, M.: 2016, The appearance of spicules in high resolution observations of Ca II H and Hα. *Astrophys. J.* **824**, 65. DOI. ADS.

Pereira, T.M.D., De Pontieu, B., Carlsson, M., Hansteen, V., Tarbell, T.D., Lemen, J., Title, A., Boerner, P., Hurlburt, N., Wülser, J.P., Martínez-Sykora, J., Kleint, L., Golub, L., McKillop, S., Reeves, K.K., Saar, S., Testa, P., Tian, H., Jaeggli, S., Kankelborg, C.: 2014, An interface region imaging spectrograph first view on solar spicules. *Astrophys. J. Lett.* **792**, L15. DOI. ADS.

Peter, H.: 2001, On the nature of the transition region from the chromosphere to the corona of the Sun. *Astron. Astrophys.* **374**, 1108. DOI. ADS.

Pike, C.D., Harrison, R.A.: 1997, EUV observations of a macrospicule: Evidence for solar wind acceleration? *Solar Phys.* **175**, 457. DOI. ADS.

Pneuman, G.W., Kopp, R.A.: 1978, Downflow in the supergranulation network and its implications for transition region models. *Solar Phys.* **57**, 49. DOI. ADS.

Puschmann, K.G.: 2016a, Spicules and their on-disk counterparts, the main driver for solar chromospheric heating? arXiv. ADS.

Puschmann, K.G.: 2016b, The GREGOR Fabry–Pérot Interferometer (GFPI). Technical Innovations and Results achieved in 2013. arXiv. ADS.

Puschmann, K.G., Beck, C.: 2011, Application of speckle and (multi-object) multi-frame blind deconvolution techniques on imaging and imaging spectropolarimetric data. *Astron. Astrophys.* **533**, A21. DOI. ADS.

Puschmann, K.G., Kneer, F., Seelemann, T., Wittmann, A.D.: 2006, The new Göttingen Fabry–Pérot spectrometer for two-dimensional observations of the Sun. *Astron. Astrophys.* **451**, 1151. DOI. ADS.

Puschmann, K.G., Kneer, F., Nicklas, H., Wittmann, A.D.: 2007, From the "Göttingen" Fabry–Pérot Interferometer to the GREGOR FPI. In: Kneer, F., Puschmann, K.G., Wittmann, A.D. (eds.) *Modern Solar Facilities – Advanced Solar Science*, Universitätsverlag, Göttingen, 45. ADS.

Puschmann, K.G., Balthasar, H., Bauer, S.-M., Hahn, T., Popow, E., Seelemann, T., Volkmer, R., Woche, M., Denker, C.: 2012a, The GREGOR Fabry–Pérot interferometer: A new instrument for high-resolution spectropolarimetric solar observations. In: Rimmele, T.R., Tritschler, A., Wöger, F., Collados Vera, M., Socas-Navarro, H., Schlichenmaier, R., Carlsson, M., Berger, T., Cadavid, A., Gilbert, P.R., Goode, P.R., Knölker, M. (eds.) *The Second ATST-EAST Meeting: Magnetic Fields from the Photosphere to the Corona*, *Astron. Soc. Pacific Conf. Ser.* **463**, 423. ADS.

Puschmann, K.G., Balthasar, H., Beck, C., Louis, R.E., Popow, E., Seelemann, T., Volkmer, R., Woche, M., Denker, C.: 2012b, The GREGOR Fabry–Pérot interferometer: Status report and prospects. In: *Ground-Based and Airborne Instrumentation for Astronomy IV*, *SPIE Conf. Ser.* **8446**, 79. DOI. ADS.

Puschmann, K.G., Denker, C., Kneer, F., Al Erdogan, N., Balthasar, H., Bauer, S.M., Beck, C., Bello González, N., Collados, M., Hahn, T., Hirzberger, J., Hofmann, A., Louis, R.E., Nicklas, H., Okunev, O., Martínez Pillet, V., Popow, E., Seelemann, T., Volkmer, R., Wittmann, A.D., Woche, M.: 2012c, The GREGOR Fabry–Pérot Interferometer. *Astron. Nachr.* **333**, 880. DOI. ADS.

Puschmann, K.G., Denker, C., Balthasar, H., Louis, R.E., Popow, E., Woche, M., Beck, C., Seelemann, T., Volkmer, R.: 2013, GREGOR Fabry–Pérot interferometer and its companion the blue imaging solar spectrometer. *Opt. Eng.* **52**(8), 081606. DOI. ADS.

Ramelli, R., Bianda, M., Merenda, L., Trujillo Bueno, T.: 2006, The Hanle and Zeeman effects in solar spicules. In: Casini, R., Lites, B.W. (eds.) *Proc. SPW4*, *Astron. Soc. Pacific Conf. Ser.* **358**, 448. ADS.

Reardon, K.P., Cavallini, F.: 2008, Characterization of Fabry–Pérot interferometers and multi-etalon transmission profiles. The IBIS instrumental profile. *Astron. Astrophys.* **481**, 897. DOI. ADS.

Rimmele, T.R., Wagner, J., Keil, S., Elmore, D., Hubbard, R., Hansen, E., Warner, M., Jeffers, P., Phelps, L., Marshall, H., Goodrich, B., Richards, K., Hegwer, S., Kneale, R., Ditsler, J.: 2010, The advanced technology solar telescope: Beginning construction of the world's largest solar telescope. In: Stepp, L.M., Gilmozzi, R., Hall, H.J. (eds.) *Ground-Based and Airborne Telescopes III*, *SPIE Conf. Ser.* **7733**. DOI. ADS.

Roberts, W.O.: 1945, A preliminary report on chromospheric spicules of extremely short lifetime. *Astrophys. J.* **101**, 136. DOI. ADS.

Rouppe van der Voort, L.H.M., De Pontieu, B., Hansteen, V.H., Carlsson, M., van Noort, M.: 2007, Magnetoacoustic shocks as a driver of quiet-Sun mottles. *Astrophys. J. Lett.* **660**, L169. DOI. ADS.

Rouppe van der Voort, L., Leenaarts, J., de Pontieu, B., Carlsson, M., Vissers, G.: 2009, On-disk counterparts of type II spicules in the Ca II 854.2 nm and Hα lines. *Astrophys. J.* **705**, 272. DOI. ADS.

Rouppe van der Voort, L., De Pontieu, B., Pereira, T.M.D., Carlsson, M., Hansteen, V.: 2015, Heating signatures in the disk counterparts of solar spicules in interface region imaging spectrograph observations. *Astrophys. J. Lett.* **799**, L3. DOI. ADS.

Rutten, R.J., Stencel, R.E.: 1980, Solar limb emission lines near CA II H & K and their spatial intensity variations. *Astron. Astrophys. Suppl.* **39**, 415. ADS.

Sánchez-Andrade Nuño, B., Centeno, R., Puschmann, K.G., Trujillo Bueno, J., Blanco Rodríguez, J., Kneer, F.: 2007, Spicule emission profiles observed in He I 10 830 Å. *Astron. Astrophys.* **472**, L51. DOI. ADS.

Sánchez-Andrade Nuño, B., Bello González, N., Blanco Rodríguez, J., Kneer, F., Puschmann, K.G.: 2008, Fast events and waves in an active region of the Sun observed in Hα with high spatial resolution. *Astron. Astrophys.* **486**, 577. DOI. ADS.

Scharmer, G.B., Bjelksjo, K., Korhonen, T.K., Lindberg, B., Petterson, B.: 2003, The 1-meter Swedish solar telescope. In: Keil, S.L., Avakyan, S.V. (eds.) *Innovative Telescopes and Instrumentation for Solar Astrophysics*, *SPIE Conf. Ser.* **4853**, 341. ADS.

Scharmer, G.B., Narayan, G., Hillberg, T., de la Cruz Rodriguez, J., Löfdahl, M.G., Kiselman, D., Sütterlin, P., van Noort, M., Lagg, A.: 2008, CRISP spectropolarimetric imaging of penumbral fine structure. *Astrophys. J. Lett.* **689**, L69. DOI. ADS.

Schmidt, W., Fisher, J.: 2013, Dynamics of the Fe II 396.94 nm emission line observed at solar disk center. *Astron. Astrophys.* **560**, A50. DOI. ADS.

Schroeter, E.H., Soltau, D., Wiehr, E.: 1985, The German solar telescopes at the Observatorio del Teide. *Vistas Astron.* **28**, 519. DOI. ADS.

Scullion, E., Doyle, J.G., Erdélyi, R.: 2010, A spectroscopic analysis of macrospicules. *Mem. Soc. Astron. Ital.* **81**, 737. ADS.

Sekse, D.H., Rouppe van der Voort, L., De Pontieu, B.: 2012, Statistical properties of the disk counterparts of type II spicules from simultaneous observations of rapid blueshifted excursions in Ca II 8542 and Hα. *Astrophys. J.* **752**, 108. DOI. ADS.

Sekse, D.H., Rouppe van der Voort, L., De Pontieu, B.: 2013, On the temporal evolution of the disk counterpart of type II spicules in the quiet Sun. *Astrophys. J.* **764**, 164. DOI. ADS.
Shibata, K., Suematsu, Y.: 1982, Why are spicules absent over plages and long under coronal holes. *Solar Phys.* **78**, 333. DOI. ADS.
Shoji, M., Nishikawa, T., Kitai, R., Ueno, S.: 2010, Spectroscopic studies of limb spicules. I. Radial and turbulent velocities. *Publ. Astron. Soc. Japan* **62**. DOI. ADS.
Skogsrud, H., Rouppe van der Voort, L., De Pontieu, B., Pereira, T.M.D.: 2015, On the temporal evolution of spicules observed with IRIS, SDO, and hinode. *Astrophys. J.* **806**, 170. DOI. ADS.
Skumanich, A., Lites, B.W., Pillet, V.M., Seagraves, P.: 1997, The calibration of the advanced Stokes polarimeter. *Astrophys. J. Suppl.* **110**, 357. DOI. ADS.
Socas-Navarro, H., Elmore, D.: 2005, Physical properties of spicules from simultaneous spectropolarimetric observations of He I and Ca II lines. *Astrophys. J. Lett.* **619**, L195. DOI. ADS.
Socas-Navarro, H., Elmore, D., Pietarila, A., Darnell, A., Lites, B.W., Tomczyk, S., Hegwer, S.: 2006, Spinor: Visible and infrared spectro-polarimetry at the National Solar Observatory. *Solar Phys.* **235**, 55. DOI. ADS.
Staveland, L.: 1970, Determination of the spread function for solar stray light. *Solar Phys.* **12**, 328. DOI. ADS.
Stellmacher, G., Wiehr, E.: 1981, On the branching in the emission relations of Ca^{+} in prominences. *Solar Phys.* **71**, 299. DOI. ADS.
Stellmacher, G., Wiehr, E.: 2015, Non-thermal line-broadening in solar prominences. *Astron. Astrophys.* **581**, A141. DOI. ADS.
Stellmacher, G., Wiehr, E., Dammasch, I.E.: 2003, Spectroscopy of solar prominences simultaneously from space and ground. *Solar Phys.* **217**, 133. DOI. ADS.
Sterling, A.C.: 2000, Solar spicules: A review of recent models and targets for future observations (Invited Review). *Solar Phys.* **196**, 79. DOI. ADS.
Sterling, A.C., Moore, R.L., DeForest, C.E.: 2010, Hinode solar optical telescope observations of the source regions and evolution of "type II" spicules at the solar polar limb. *Astrophys. J. Lett.* **714**, L1. DOI. ADS.
Suematsu, Y.: 1998, Solar spicules: A brief review of recent high-resolution observations. In: Guyenne, T.-D. (ed.) *Solar Jets and Coronal Plumes*, *ESA* **SP 421**, 19. ADS.
Suematsu, Y., Wang, H., Zirin, H.: 1995, High-resolution observation of disk spicules. I. Evolution and kinematics of spicules in the enhanced network. *Astrophys. J.* **450**, 411. DOI. ADS.
Suematsu, Y., Shibata, K., Neshikawa, T., Kitai, R.: 1982, Numerical hydrodynamics of the jet phenomena in the solar atmosphere. I – Spicules. *Solar Phys.* **75**, 99. DOI. ADS.
Suematsu, Y., Katsukawa, Y., Ichimoto, K., Tsuneta, S., Okamoto, T., Nagata, S., Shimizu, T., Tarbell, T., Shine, R., Title, A.: 2007, High resolution observation of spicules in Ca II H with hinode/SOT. In: *Bull. American Astron. Soc.* **39**, 219. ADS.
Suematsu, Y., Ichimoto, K., Katsukawa, Y., Shimizu, T., Okamoto, T., Tsuneta, S., Tarbell, T., Shine, R.A.: 2008, High resolution observations of spicules with hinode/SOT. In: Matthews, S.A., Davis, J.M., Harra, L.K. (eds.) *First Results from Hinode*, *Astron. Soc. Pacific Conf. Ser.* **397**, 27. ADS.
Tandberg-Hanssen, E.: 1960, An investigation of the temperature conditions in prominences with a special study of the excitation of helium. *Astrophys. Nor.* **6**, 161. ADS.
Tian, H., McIntosh, S.W., De Pontieu, B., Martínez-Sykora, J., Sechler, M., Wang, X.: 2011, Two components of the solar coronal emission revealed by extreme-ultraviolet spectroscopic observations. *Astrophys. J.* **738**, 18. DOI. ADS.
Tian, H., DeLuca, E.E., Cranmer, S.R., De Pontieu, B., Peter, H., Martínez-Sykora, J., Golub, L., McKillop, S., Reeves, K.K., Miralles, M.P., McCauley, P., Saar, S., Testa, P., Weber, M., Murphy, N., Lemen, J., Title, A., Boerner, P., Hurlburt, N., Tarbell, T.D., Wuelser, J.P., Kleint, L., Kankelborg, C., Jaeggli, S., Carlsson, M., Hansteen, V., McIntosh, S.W.: 2014, Prevalence of small-scale jets from the networks of the solar transition region and chromosphere. *Science* **346**(27), 1255711. DOI. ADS.
Tritschler, A., Schmidt, W., Langhans, K., Kentischer, T.: 2002, High-resolution solar spectroscopy with TESOS – Upgrade from a double to a triple system. *Solar Phys.* **211**, 17. DOI. ADS.
Trujillo Bueno, J., Merenda, L., Centeno, R., Collados, M., Landi Degl'Innocenti, E.: 2005, The Hanle and Zeeman effects in solar spicules: A novel diagnostic window on chromospheric magnetism. *Astrophys. J. Lett.* **619**, L191. DOI. ADS.
Tsiropoula, G., Schmieder, B.: 1997, Determination of physical parameters in dark mottles. *Astron. Astrophys.* **324**, 1183. ADS.
Tsiropoula, G., Tziotziou, K., Kontogiannis, I., Madjarska, M.S., Doyle, J.G., Suematsu, Y.: 2012, Solar fine-scale structures. I. Spicules and other small-scale, jet-like events at the chromospheric level: Observations and physical parameters. *Space Sci. Rev.* **169**, 181. DOI. ADS.
Tsuneta, S., Ichimoto, K., Katsukawa, Y., Nagata, S., Otsubo, M., Shimizu, T., Suematsu, Y., Nakagiri, M., Noguchi, M., Tarbell, T., Title, A., Shine, R., Rosenberg, W., Hoffmann, C., Jurcevich, B., Kushner,

G., Levay, M., Lites, B., Elmore, D., Matsushita, T., Kawaguchi, N., Saito, H., Mikami, I., Hill, L.D., Owens, J.K.: 2008, The solar optical telescope for the hinode mission: An overview. *Solar Phys.* **249**, 167. DOI. ADS.

van Noort, M., Rouppe van der Voort, L., Löfdahl, M.G.: 2005, Solar image restoration by use of multi-frame blind de-convolution with multiple objects and phase diversity. *Solar Phys.* **228**, 191. DOI. ADS.

von der Lühe, O., Soltau, D., Berkefeld, T., Schelenz, T.: 2003, KAOS: Adaptive optics system for the vacuum tower telescope at Teide Observatory. In: Keil, S.L., Avakyan, S.V. (eds.) *Innovative Telescopes and Instrumentation for Solar Astrophysics*, *SPIE Conf. Ser.* **4853**, 187. ADS

Watanabe, T., Steenbock, W.: 1986, Fe II emission lines in the wings of CA II H and K. I – Solar Fe II 3969.4 A line. *Astron. Astrophys.* **165**, 163. ADS.

Yurchyshyn, V., Abramenko, V., Goode, P.: 2013, Dynamics of chromospheric upflows and underlying magnetic fields. *Astrophys. J.* **767**, 17. DOI. ADS.

Zachariadis, T.G., Georgakilas, A.A., Koutchmy, S., Alissandrakis, C.E., Dara, H.C.: 1999, Fine structure of the solar chromosphere: Arch-shaped mottles. *Solar Phys.* **184**, 77. DOI. ADS.

Zhang, Y.Z., Shibata, K., Wang, J.X., Mao, X.J., Matsumoto, T., Liu, Y., Su, J.T.: 2012, Revision of solar spicule classification. *Astrophys. J.* **750**, 16. DOI. ADS.

Zirin, H.: 1988, *Astrophysics of the Sun*, Cambridge University Press, Cambridge.

Zirker, J.B.: 1962a, On the brightness of chromospheric spicules. *Astrophys. J.* **135**, 515. DOI. ADS.

Zirker, J.B.: 1962b, Spectral observations of solar chromospheric spicules. *Astrophys. J.* **136**, 250. DOI. ADS.

Zwaan, C.: 1965, Sunspot models: A study of sunspot spectra. In: *Recherches Astronomiques de L'Observatoire D'Utrecht* **17**, *Dordrecht, Netherlands*.